

Alignment destabilizes crystal order in active systemsChen Huang ¹, Leiming Chen,² and Xiangjun Xing ^{1,3,4,*}¹*Wilczek Quantum Center, School of Physics and Astronomy, Shanghai Jiao Tong University, Shanghai 200240 China*²*School of Materials Science and Physics, China University of Mining and Technology, Xuzhou, Jiangsu, 221116 China*³*Tsung-Dao Lee Institute, Shanghai Jiao Tong University, Shanghai 200240 China*⁴*Shanghai Research Center for Quantum Sciences, Shanghai 201315 China*

(Received 30 March 2021; revised 30 July 2021; accepted 4 November 2021; published 9 December 2021)

We combine numerical and analytical methods to study two-dimensional active crystals formed by permanently linked swimmers and with two distinct alignment interactions. The system admits a stationary phase with quasi-long-range translational order, as well as a moving phase with quasi-long-range active force director and velocity order. The translational order in the moving phase is significantly influenced by alignment interaction. For Vicsek-like alignment, the translational order is short ranged, whereas the bond-orientational order is quasi-long ranged, implying a moving hexatic phase. For elasticity-based alignment, the translational order is quasi-long ranged parallel to the motion and short ranged in the perpendicular direction, whereas the bond orientational order is long ranged. We also generalize these results to higher dimensions.

DOI: [10.1103/PhysRevE.104.064605](https://doi.org/10.1103/PhysRevE.104.064605)**I. INTRODUCTION**

One of the most interesting and fundamental issues about active systems [1–6] is the stability of orders. According to the Mermin-Wagner theorem [7], two-dimensional (2D) equilibrium systems with continuous symmetry and short-range interaction cannot exhibit long-range order (LRO). However, LRO was discovered in 2D polar active fluid both in simulation [8] and in hydrodynamic theory [9–12]. This LRO is accompanied by super-diffusion and giant number fluctuations [2,6,11,13], neither of which is seen in equilibrium systems with short-range interactions. Many variants of Vicsek models with different particle polarity, alignments, and exclusion [12–26] have been studied, and a variety of novel phenomena have been discovered.

Dense active systems with repulsive interactions may also exhibit translational orders. Solid phases as well as fluid-solid phase separations have been repeatedly observed in active colloidal systems both experimentally [27–29] and numerically [30–34]. In most of these works, there is no alignment interaction and no visible collective motion. More recently, Weber *et al.* [20] simulated a model of active crystal with Vicsek-type alignment and discovered a stationary phase with quasi-long-range (QLR) translational order, as well as a phase of moving crystal domains separated by grain boundaries.¹ Very recently, Maitra *et al.* [35] studied an active generalization of nematic elastomer [36] with spontaneous breaking of rotational symmetry [37,38] and found QLR translational orders in 2D. Their elastic energy contains a hidden rotational symmetry (and its resulting Goldstone modes) involving both

shear deformation and orientational order, which are difficult to realize experimentally.

Regardless of many previous studies, it is not clear whether there exists a moving phase with certain translational order in active systems with alignment interactions if the soft-mode in Ref. [35] does not come into play. To address this interesting question, here we combine analytic and numerical approaches to study a model system of active crystal consisting of a 2D triangular array of swimmers linked permanently by springs. We introduce alignment interaction between neighboring swimmers that is either Vicsek-like (AD-I) or elasticity based [39,40] (AD-II). In the strong noise–weak alignment regime, we find a stationary phase with QLR translational order, which was also seen in Refs. [20,41]. In the weak noise–strong alignment regime we find a moving phase with QLR active force director and velocity order and with the nature of translational order depending on the alignment. For AD-I, the moving phase exhibits only short-range (SR) translational order and QLR bond orientational order and hence should be identified as a *moving hexatic phase*. For AD-II, the translational order is QLR along the moving direction, and SR in the perpendicular direction, whereas the bond-orientational order is LR. We generalize the model to higher dimensions and show that the active force director alignment in active systems tends to destabilize crystal orders.

There are many experimental realizations of the models studied in this work. Vicsek-like alignment, for example, is believed to be relevant for living matters and flocking behaviors [2,4–6]. It may also be realized effectively as a consequence of collision [42] or interaction [43] between active particles or in micro-robotics using remote-sensing [44–46]. Both harmonic potential interaction and elasticity-based alignment interactions may be realized by remote sensing of the directions or positions between programmed robotics [44–46]. Finally, it is also conceivable to link

*xxing@sjtu.edu.cn

¹Note, however, that in this work the dynamical equations contain no noise term.

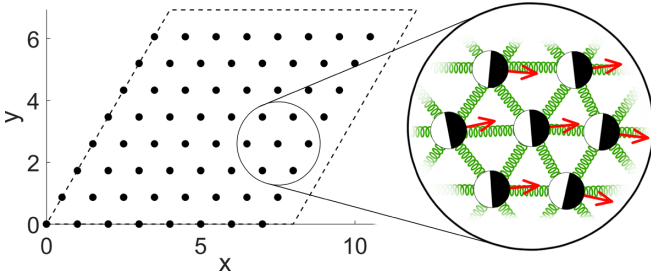


FIG. 1. Our simulation model. Swimmers are connected by springs and driven by active forces, shown as red arrows.

swimmers using polymers and to induce alignment interactions using hydrodynamic effects or magnetic interactions. The remainder of this work is organized as follows. In Sec. II we present the simulation models and details. In Sec. III we present numerical results on phase diagram and various correlation functions both in the stationary phase and in the moving phase. In Sec. IV we analytically study the models and show that the results are fully consistent with the simulation results. In Sec. V we draw concluding remarks. In the Appendices, we present various details of simulations and analytic calculations.

II. MODEL AND SIMULATION DETAILS

As schematized in Fig. 1, our simulation model consists of a triangular array of N swimmers connected permanently by harmonic springs. Each swimmer moves under the influences of elastic force, friction and noise, as well as active force. The position $\mathbf{r}_i(t)$ of the i th swimmer in the laboratory frame obeys the following overdamped Langevin equation:

$$\gamma_p \dot{\mathbf{r}}_i(t) = b_p \mathbf{n}(\theta_i) + \mathbf{F}_i(t) + \gamma_p \sqrt{2D_p} \boldsymbol{\xi}_i(t), \quad (1)$$

where γ_p is the friction coefficient and $b_p \mathbf{n}(\theta_i)$ is the active force with fixed magnitude b_p and director $\mathbf{n}(\theta_i)$. The angle $\theta_i(t)$ is defined with respect to the $\hat{\mathbf{x}}$ axis, and is related to $\mathbf{n}(\theta_i)$ via $\mathbf{n}(\theta_i) = (\cos \theta_i, \sin \theta_i)$. Throughout this section, we use symbols with subscript p to denote parameters of the particle model in order to distinguish them from the parameters of the continuum model to be discussed in Sec. IV.

The second term in right-hand side of Eq. (1) is the elastic force, given by

$$\mathbf{F}_i = \sum_{j \text{ n.n. } i} \kappa (|\mathbf{r}_i - \mathbf{r}_j| - a_0) \frac{\mathbf{r}_i - \mathbf{r}_j}{|\mathbf{r}_i - \mathbf{r}_j|}, \quad (2)$$

where the summation is over six nearest neighbors of swimmer i , while κ and a_0 are respectively the elastic constant and natural length of the springs. The last term of Eq. (1) is the random force, with $\boldsymbol{\xi}_i(t)$ the unit-variance Gaussian white noise. The translational diffusion coefficient D_p satisfies the Einstein relation $D_p = T/\gamma_p$, where T is the temperature of ambient fluid with the Boltzmann constant $k_B = 1$.

We consider two distinct alignment dynamics for the active forces. The first alignment dynamics (AD-I) is Vicsek-like [8], with each swimmer trying to align its director of active force

with its neighbors,² subject to an internal noise:

$$\dot{\theta}_i(t) = g_p (\mathbf{n}(\theta_i) \times \langle \mathbf{n} \rangle_i) \cdot \hat{\mathbf{z}} + \sqrt{2D_p^\theta} \eta_i(t), \quad (\text{AD-I})$$

where g_p is the alignment strength for (AD-I), $\hat{\mathbf{z}}$ is the unit normal to the plane, $\langle \mathbf{n} \rangle_i \equiv \sum_{j \text{ n.n. } i} \mathbf{n}(\theta_j)/6$ is the average director of all the six nearest neighbors, D_p^θ is the rotational diffusion coefficient, and $\eta_i(t)$ is a unit Gaussian white noise. Equation (AD-I) describes the alignment of the active force of each particle with those of its nearest neighbors. This alignment mechanism by perceiving the average orientation of neighbors has already been realized in swarm robots [44–46]. It may also be realized in self-propelling Janus colloids that are able to align directions [43].

The second alignment dynamics (AD-II) is elasticity based [39,40,47], with each swimmer aligning its active force with the local elastic force, so as to reduce the local elastic energy:

$$\dot{\theta}_i(t) = c_p (\mathbf{n}(\theta_i) \times \mathbf{F}_i) \cdot \hat{\mathbf{z}} + \sqrt{2D_p^\theta} \eta_i(t), \quad (\text{AD-II})$$

where c_p is the alignment strength. This mechanism can be implemented, either by directly installing force sensors on active particles or swarm robots or by indirect visual perception of their relative positions [44–46].

A. Dimensionless forms and choice of parameters

Here we define various dimensionless parameters and variables and rewrite the dynamical equations in dimensionless forms suitable for numerical computation. We use the lattice constant a_0 as a unit of length and denote an arbitrary time unit as τ_0 . The dimensionless parameters and variables are defined as:

$$\begin{aligned} \tilde{\mathbf{r}} &\equiv \mathbf{r}/a_0, \\ \tilde{b}_p &\equiv b\tau_0/(\gamma a_0), & \tilde{\kappa} &\equiv \kappa\tau_0/\gamma, & \tilde{D}_p &\equiv D\tau_0/a_0^2, \\ \tilde{D}_p^\theta &\equiv D_\theta\tau_0, & \tilde{g}_p &\equiv g_p\tau_0, & \tilde{c}_p &\equiv c\gamma a_0, \\ \tilde{\mathbf{F}}_i &\equiv \mathbf{F}_i\tau_0/(\gamma a_0), & \tilde{\eta}_i &\equiv \eta\sqrt{\tau_0}, & \tilde{\boldsymbol{\xi}}_i &\equiv \boldsymbol{\xi}\sqrt{\tau_0}. \end{aligned} \quad (3)$$

The dimensionless form of Eq. (1) is

$$\dot{\tilde{\mathbf{r}}}_i(\tilde{t}) = \tilde{b}_p \mathbf{n}(\theta_i) + \tilde{\mathbf{F}}_i(\tilde{t}) + \sqrt{2\tilde{D}_p} \tilde{\boldsymbol{\xi}}_i(\tilde{t}). \quad (4)$$

The dimensionless forms of the alignment dynamics are as follows:

$$\dot{\theta}_i(\tilde{t}) = \tilde{g}_p (\mathbf{n}(\theta_i) \times \langle \mathbf{n} \rangle_i) \cdot \hat{\mathbf{z}} + \sqrt{2\tilde{D}_p^\theta} \tilde{\eta}_i, \quad (\text{AD-}\tilde{\text{I}})$$

$$\dot{\theta}_i(\tilde{t}) = \tilde{c}_p (\mathbf{n}(\theta_i) \times \tilde{\mathbf{F}}_i) \cdot \hat{\mathbf{z}} + \sqrt{2\tilde{D}_p^\theta} \tilde{\eta}_i. \quad (\text{AD-}\tilde{\text{II}})$$

We use a rhombic cell with periodic boundary condition (cf. Fig. 1) and numerically integrate the dynamical equations, Eq. (4), (AD- $\tilde{\text{I}}$), and (AD- $\tilde{\text{II}}$), using the first-order Euler-Maruyama scheme [48]. The discretized equations are shown in Appendix A, with the simulation time step $\Delta\tilde{t} = 10^{-3}$.

²Note that in the original Vicsek model [8], swimmers control their velocities instead of active forces. In the overdamped regime, this difference is inessential.

We choose the parameters $\tilde{b}_p = 2$, $\tilde{\kappa} = 100$ for AD-I and $\tilde{\kappa} = 20$ for AD-II. The dimensionless translational diffusion coefficient is chosen to be $\tilde{D}_p = 0.01$. The value of \tilde{g}_p , \tilde{c}_p , and \tilde{D}_p^θ are specified in the following sections, respectively. Numerical results indicate that, with these choices of parameters, the system is in the small deformation regime.

III. NUMERICAL RESULTS

A. Phase diagram

We define the order parameter $P = \langle |\frac{1}{N} \sum_k \mathbf{n}(\theta_k)| \rangle_t$, which is the steady-state time average of the magnitude of the system-averaged active force director. Summing Eq. (1) over all swimmers, we see that the elastic forces vanish because of Newton's third law, and hence we obtain $b_p |\frac{1}{N} \sum_k \mathbf{n}(\theta_k)| = \gamma_p |\frac{1}{N} \sum_k \dot{\mathbf{r}}_i(t) - \frac{1}{N} \sqrt{2\tilde{D}_p} \sum_k \xi_i(t)|$. For infinite system size, the sum over noises converges to zero according to the law of large numbers, and we see that the order parameter is strictly proportional to the absolute value of average velocity of all swimmers, further averaged over time. Hence for infinite system size, the order parameter can be used to distinguish the stationary phase ($P = 0$) from the moving phase ($P \neq 0$). For finite system size, the proportionality between P and the average velocity of the system is only approximate. Nonetheless, we can obtain a good estimate of the phase boundary by simulating systems with sizes 32×32 and 64×64 .

As shown in Fig. 2(a), for weak alignment–strong active noise (dark blue in upper left) there is a stationary phase where P is approximately zero,³ whereas for strong alignment–weak active noise (bright yellow in lower right) there is a collectively moving phase where P is finite. As shown in Fig. 2(b), fitting of P as a function of alignment strength for a relatively larger system size 64×64 suggests that these two phases are separated by a line of second-order phase transitions.

B. Definitions of correlation functions

In this subsection we define various correlation functions in an active crystal.

We first define the displacement vector field $\tilde{\mathbf{u}}_i$ (in dimensionless units) as the deviation from the perfect lattice location of each particle i , either in the laboratory frame for the stationary phase or in the comoving frame for the moving phase. Then we numerically Fourier transform the displacement vector field $\tilde{\mathbf{u}}$ into the reciprocal \mathbf{k} -space vector field $\hat{\mathbf{u}}(\mathbf{k}) = (\hat{u}_x(\mathbf{k}), \hat{u}_y(\mathbf{k}))$, where $\mathbf{k} = (k_x, k_y)$ is the dimensionless wave vector reciprocal to the dimensionless distances. We compute averages of the norm squared $\langle |\hat{u}_x(\mathbf{k})|^2 \rangle$, $\langle |\hat{u}_y(\mathbf{k})|^2 \rangle$, which will be hereafter referred to as the \mathbf{u} -correlations (in momentum space). The technical details of numerical Fourier transformation on the triangular lattice are presented in Appendix B.

The real-space translational correlation function $g_{\mathbf{q}}(\tilde{r})$ for a lattice characterizes the correlation of translational order with Bragg vector $\mathbf{q} = (q_x, q_y)$ at two regions separated by

³It is never strictly zero because the system is finite and there are always instantaneous fluctuations at each time.

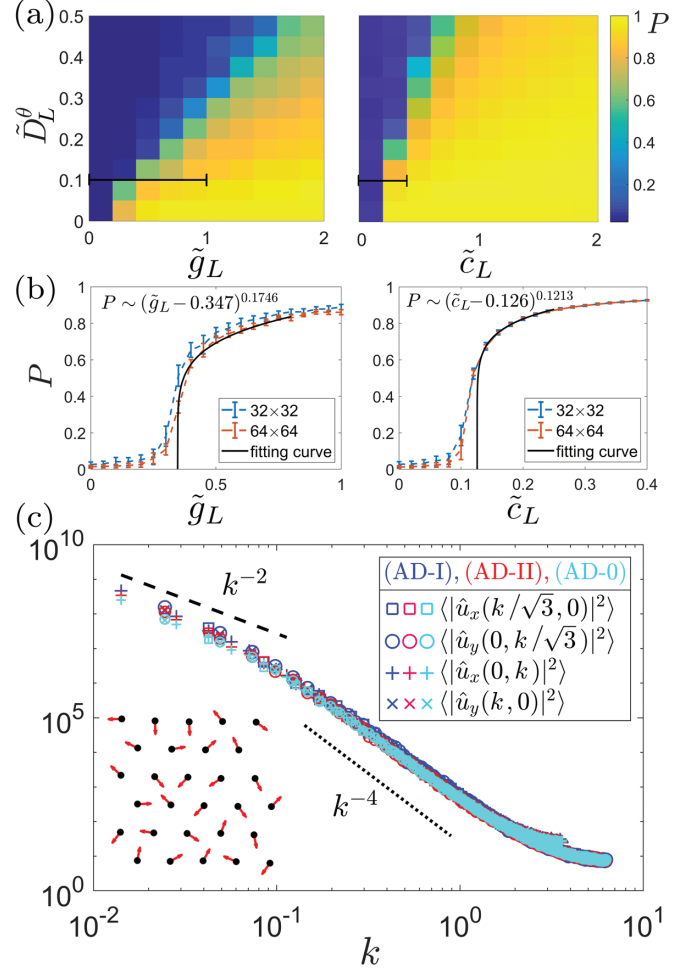


FIG. 2. (a) Phase diagram of AD-I (left) and AD-II (right). Vertical axis: Dimensionless noise strength \tilde{D}_p^θ ; horizontal axis: dimensionless alignment \tilde{g}_p (AD-I) or \tilde{c}_p (AD-II). The color represents the order parameter of average alignment P , defined in the main text. (b) Average alignment P of AD-I (left) and AD-II (right) as a function of alignment interaction strength, from a cut indicated by the black line segments in (a), suggests second-order phase transitions. The fitting is applied on the curve of system size 64×64 . (c) Log-log plot of the \mathbf{u} correlations $\langle |\hat{u}_x|^2 \rangle$ and $\langle |\hat{u}_y|^2 \rangle$ of the stationary phase along the \hat{k}_x and \hat{k}_y axis, with parameters $\tilde{b}_p = 2$, $\tilde{D}_p = 0.01$, $\tilde{D}_p^\theta = 0.3$, $(\tilde{\kappa}, \tilde{g}_p) = (100, 0.1)$ in AD-I, $(\tilde{\kappa}, \tilde{c}_p) = (20, 0.1)$ in AD-II, and $(\tilde{\kappa}, \tilde{g}_p, \tilde{c}_p) = (100, 0, 0)$ in AD-0. Bottom left inset: A typical configuration of active forces in the stationary phase.

a dimensionless distance $\tilde{r} \equiv r/a_0$ [49]:

$$g_{\mathbf{q}}(\tilde{r}) = \frac{\sum_{j \neq k} \zeta(\tilde{r} - |\tilde{\mathbf{r}}_j - \tilde{\mathbf{r}}_k|) \text{Re}(e^{i\mathbf{q} \cdot (\tilde{\mathbf{r}}_j - \tilde{\mathbf{r}}_k)})}{2\pi \tilde{r} \Delta \tilde{r} \rho N}, \quad (5)$$

where $\tilde{\mathbf{r}}_j = (\tilde{x}_j, \tilde{y}_j)$ is the dimensionless Cartesian coordinates of the j th particle and $\zeta = 1$ if the distance $|\tilde{\mathbf{r}}_j - \tilde{\mathbf{r}}_k|$ is in the interval $\tilde{r} \sim \tilde{r} + \Delta \tilde{r}$; otherwise, $\zeta = 0$. The number density $\rho = (\sqrt{3}/2)^{-1}$ is the inverse of the area of a unit cell in the triangular lattice of unit length. The dimensionless reciprocal vector \mathbf{q} is evaluated as the Bragg peaks of the structure factor:

$$Q(q_x, q_y) = \frac{1}{N} \langle \rho(q_x, q_y) \rho(-q_x, -q_y) \rangle, \quad (6)$$

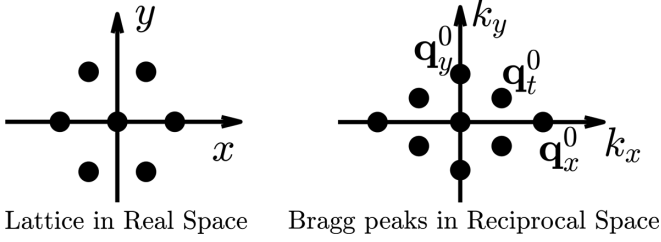


FIG. 3. The perfect triangular lattice in real space (left) and its corresponding Bragg peaks in the reciprocal space (right). Only parts of the lattices near the origin are displayed. In dimensionless length scales, the real-space lattice has unit lattice constant, while the reciprocal lattice has lattice spacing $2\pi/(\sqrt{3}/2)$. The symbols \mathbf{q}_x^0 , \mathbf{q}_y^0 , and \mathbf{q}_t^0 are defined in Sec. III D.

where

$$\rho(q_x, q_y) = \sum_{j=1}^N \exp[i(q_x \tilde{x}_j + q_y \tilde{y}_j)]. \quad (7)$$

The Bragg peaks of a perfect triangular lattice also form a perfect triangular lattice in the reciprocal space, see Fig. 3. However, as demonstrated in Ref. [49], because of sample-to-sample fluctuations of crystal structure, the Bragg peak \mathbf{q} of $g_{\mathbf{q}}(\tilde{\mathbf{r}})$ must be identified carefully as the peak value of each sample state, i.e., the true Bragg peaks are near but not exactly equal to the Bragg peaks of a perfect hexagonal lattice.

The correlation function of the active force director is defined as $\langle \mathbf{n}(0) \cdot \mathbf{n}(\tilde{\mathbf{r}}) \rangle_c \equiv \langle (\mathbf{n}(0) - \langle \mathbf{n} \rangle) \cdot (\mathbf{n}(\tilde{\mathbf{r}}) - \langle \mathbf{n} \rangle) \rangle = \langle \mathbf{n}(0) \cdot \mathbf{n}(\tilde{\mathbf{r}}) \rangle - \langle \mathbf{n} \rangle^2$ where the system-average director $\langle \mathbf{n} \rangle \equiv N^{-1} \sum_{i=1}^N \mathbf{n}(\theta_i)$, and

$$\langle \mathbf{n}(0) \cdot \mathbf{n}(\tilde{\mathbf{r}}) \rangle = \frac{\sum_{j \neq k} \zeta(\tilde{\mathbf{r}} - |\tilde{\mathbf{r}}_j - \tilde{\mathbf{r}}_k|) \mathbf{n}(\theta_j) \cdot \mathbf{n}(\theta_k)}{2\pi \tilde{r} \Delta \tilde{r} \rho N}. \quad (8)$$

Similarly, the velocity correlation function is defined as $\langle \hat{\mathbf{v}}(0) \cdot \hat{\mathbf{v}}(\tilde{\mathbf{r}}) \rangle_c \equiv \langle \hat{\mathbf{v}}(0) \cdot \hat{\mathbf{v}}(\tilde{\mathbf{r}}) \rangle - \langle \hat{\mathbf{v}} \rangle^2$ where the system-average unit velocity $\langle \hat{\mathbf{v}} \rangle \equiv N^{-1} \sum_{i=1}^N \hat{\mathbf{v}}_i$, and

$$\langle \hat{\mathbf{v}}(0) \cdot \hat{\mathbf{v}}(\tilde{\mathbf{r}}) \rangle = \frac{\sum_{j \neq k} \zeta(r - |\tilde{\mathbf{r}}_j - \tilde{\mathbf{r}}_k|) \hat{\mathbf{v}}_j \cdot \hat{\mathbf{v}}_k}{2\pi \tilde{r} \Delta \tilde{r} \rho N}, \quad (9)$$

and the normalized velocity is $\tilde{\mathbf{v}}_j \equiv \hat{\mathbf{v}}_j / |\tilde{\mathbf{v}}_j|$. The velocity $\tilde{\mathbf{v}}_j$ of each particle is evaluated by subtracting the coordinates of the two configurations in the laboratory frame separated by 100 simulation steps, which corresponds to a dimensionless time interval 0.1. This choice is made such that during this time interval, the random forces in Eq. (4) are mostly averaged out, yet the lattice moves very little.

The local bond orientational parameter of the particle at $\tilde{\mathbf{r}}_j$ is defined as $\psi_6(\tilde{\mathbf{r}}_j) = n^{-1} \sum_{m=1}^n \exp(i6\theta_m^j)$ where the sum runs over its n Voronoi neighbors at position $\tilde{\mathbf{r}}_m$, and θ_m^j is the angle of the bond $(\tilde{\mathbf{r}}_m - \tilde{\mathbf{r}}_j)$ relative to any fixed axis, say the $\hat{\mathbf{x}}$ axis. The bond-orientational correlation function $g_6(\tilde{\mathbf{r}})$ is then defined as [49]:

$$g_6(\tilde{\mathbf{r}}) = \text{Re} \langle \psi_6(\tilde{\mathbf{r}}_j) \psi_6^*(\tilde{\mathbf{r}}_k) \rangle \equiv \frac{\sum_{j \neq k} \zeta(\tilde{\mathbf{r}} - |\tilde{\mathbf{r}}_j - \tilde{\mathbf{r}}_k|) \text{Re}(\psi_6(\tilde{\mathbf{r}}_j) \psi_6^*(\tilde{\mathbf{r}}_k))}{2\pi \tilde{r} \Delta \tilde{r} \rho N}. \quad (10)$$

To study all the above orders in both the stationary and the moving phase in the following sections, we simulate a larger system with size 256×256 . The total number of simulation steps is 2×10^6 and simulation samples are collected every 2000 steps.

C. Correlation function in the stationary phase

In this section we study the \mathbf{u} -correlation function of the stationary phase. We choose the alignment strength $\tilde{g}_p = 0.1$ for AD-I and $\tilde{c}_p = 0.1$ for AD-II and the magnitude of the angular noise $\tilde{D}_p^\theta = 0.3$ for both. The simulation starts from a perfect triangular lattice where all the active forces orient randomly.

In Fig. 2(c) we plot $\langle |\hat{u}_x(\mathbf{k})|^2 \rangle$ and $\langle |\hat{u}_y(\mathbf{k})|^2 \rangle$ in \mathbf{k} space along the \hat{k}_x and \hat{k}_y axis in log-log scale in both AD-I and AD-II. For comparison we also plot the corresponding result for a model without any alignment (AD-0), which corresponds to $\tilde{g}_p = \tilde{c}_p = 0$ in Eqs. (AD-I) and (AD-II).

For a passive isotropic crystal at equilibrium, we have $b_p = 0$, and the \mathbf{u} correlations along the \hat{k}_x and \hat{k}_y axes [50]:

$$\begin{aligned} \langle |\hat{u}_x(k, 0)|^2 \rangle &= \frac{\gamma D}{3\lambda k^2}, & \langle |\hat{u}_x(0, k)|^2 \rangle &= \frac{\gamma D}{\lambda k^2}, \\ \langle |\hat{u}_y(k, 0)|^2 \rangle &= \frac{\gamma D}{\lambda k^2}, & \langle |\hat{u}_y(0, k)|^2 \rangle &= \frac{\gamma D}{3\lambda k^2}, \end{aligned} \quad (11)$$

which satisfy the following equalities:

$$\begin{aligned} \langle |\hat{u}_x(k/\sqrt{3}, 0)|^2 \rangle &= \langle |\hat{u}_x(0, k)|^2 \rangle \\ &= \langle |\hat{u}_y(k, 0)|^2 \rangle = \langle |\hat{u}_y(0, k/\sqrt{3})|^2 \rangle. \end{aligned} \quad (12)$$

This prompts us to plot four functions: $\langle |\hat{u}_x(k/\sqrt{3}, 0)|^2 \rangle$, $\langle |\hat{u}_y(0, k/\sqrt{3})|^2 \rangle$, $\langle |\hat{u}_x(0, k)|^2 \rangle$, and $\langle |\hat{u}_y(k, 0)|^2 \rangle$ for active crystal in the same plot and compare them with the result of equilibrium crystals. As shown Fig. 2(c), all four curves collapse onto each other. The master curve exhibits k^{-2} in the long length scales, as well as k^{-4} scaling in the intermediate length scale ($0.1 \lesssim k \lesssim 1$). The latter signifies anomalously large structure fluctuations in the real-space length scales $6a_0 \lesssim \ell \lesssim 60a_0$ that are caused by the fluctuations of active forces, where k in reciprocal space satisfies $\ell/a_0 = 2\pi/k$. At longer length scales or smaller k , the \mathbf{u} correlations crossover to k^{-2} scaling, which indicates a QLR translational order and is consistent with the simulation result obtained in Ref. [20]. The transition from k^{-4} to k^{-2} scaling is also consistent with very recent works on active solids by Caprini *et al.* [41,51,52] in the absence of explicit alignment, where the \mathbf{u} -correlation function under overdamped Langevin dynamics [41] has the form $\langle |\hat{\mathbf{u}}(\mathbf{k})|^2 \rangle \propto (k^2 + f(D^\theta)k^4)^{-1}$ with $f(D^\theta)$ antiproportional to D^θ . Hence we conclude that in the stationary phase, activity only affect the fine structure of the lattice but does not alter the QLR translational order at long length scales.

D. Correlation functions in the moving phase

We are most interested in the orders of the collective moving phase. For this phase, we choose the alignment strength $\tilde{g}_p = 10$ for AD-I and $\tilde{c}_p = 1$ for AD-II and the magnitude of the angular noise $\tilde{D}_p^\theta = 0.05$ for both such that the fluctuation of angle is small enough.

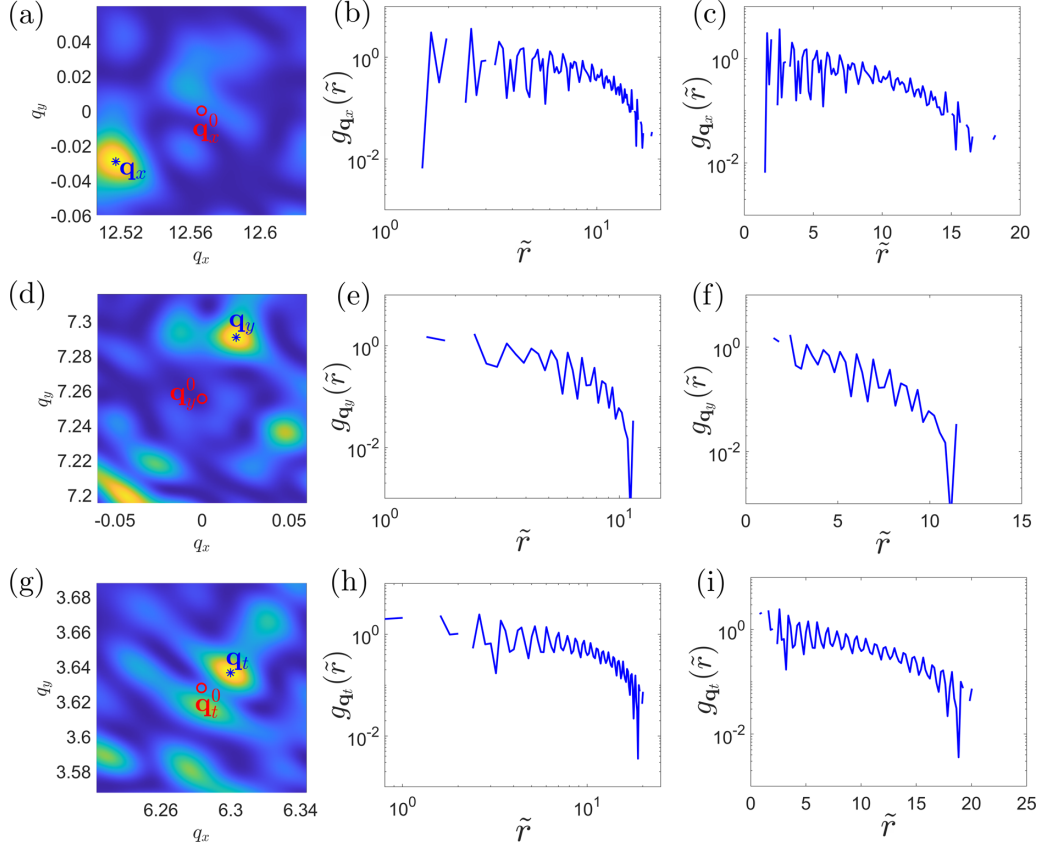


FIG. 4. Bragg peak of $Q(q_x, q_y)$ which are numerically evaluated (\mathbf{q}_x , \mathbf{q}_y , and \mathbf{q}_t) and that of a perfect hexagonal lattice (\mathbf{q}_x^0 , \mathbf{q}_y^0 , and \mathbf{q}_t^0), and the corresponding translational correlation function in AD-I with [(a)–(c)] $\mathbf{q}_x = (12.5172, -0.0292)$ and $\mathbf{q}_x^0 = (4\pi, 0)$; [(d)–(f)] $\mathbf{q}_y = (0.0196, 7.2905)$ and $\mathbf{q}_y^0 = (0, 2\pi/(\sqrt{3}/2))$; [(g)–(i)] $\mathbf{q}_t = (6.2998, 3.6363)$ and $\mathbf{q}_t^0 = 2\pi(1, 1/\sqrt{3})$. The second column is in log-log scale, while the third column is in log-linear scale.

The simulation starts again from a perfect lattice with all the active directors orienting in the positive $\hat{\mathbf{x}}$ axis, i.e., $\theta_i = 0$ for all $i \in \{1, \dots, N\}$. If we directly simulate Eqs. (AD-I) and (AD-II) for a finite system, the average velocity would evolve slowly but randomly, which complicates the computation of the translational correlation function $g_{\mathbf{q}}(\tilde{r})$ as defined in Eq. (5). This is because $g_{\mathbf{q}}(\tilde{r})$ depends both on the Bragg peak \mathbf{q} and on the average velocity, and we need a large number of data points with both of them fixed. To avoid this problem, right after each sample has been collected (per 2000 time steps), we rotate the average velocity back to the $\hat{\mathbf{x}}$ axis and then continue the simulation.

Under the constraint of collective motion along the $\hat{\mathbf{x}}$ axis, we evaluate $g_{\mathbf{q}}(\tilde{r})$ at three Bragg peaks, i.e., the first Bragg peak \mathbf{q}_y near that of a perfect triangular lattice $\mathbf{q}_y^0 = (0, 2\pi/(\sqrt{3}/2))$ along the $\hat{\mathbf{y}}$ axis (perpendicular to the collective moving direction), \mathbf{q}_t near $\mathbf{q}_t^0 = 2\pi(1, 1/\sqrt{3})$ along a tilted direction, and the second Bragg peak \mathbf{q}_x near $\mathbf{q}_x^0 = (4\pi, 0)$ along the $\hat{\mathbf{x}}$ axis (parallel to the collective moving direction), as shown in Fig. 3. Simulation data are collected after the system has reached a steady state of collective moving along the $\hat{\mathbf{x}}$ axis, with $P = 0.9915$ in AD-I and $P = 0.9830$ in AD-II.

In principle we could also choose to fix the average velocity along an arbitrary direction instead of the positive $\hat{\mathbf{x}}$ axis. The numerical computation will then become more compli-

cated, since it would be difficult to specify the corresponding Bragg peaks that are either parallel or perpendicular to this arbitrary collective moving direction. From a theoretical point of view, we do not expect the operation of constraining its motion along the $\hat{\mathbf{x}}$ axis to alter the system's long length-scale physical properties, because the long-scale continuum elasticity theory of the triangular lattice is isotropic. See the next section for more details.

We first study the translational correlation function $g_{\mathbf{q}}(\tilde{r})$ for a typical configuration of the moving phase. We plot in Figs. 4 and 5, for AD-I and AD-II, respectively, the structure factor $Q(q_x, q_y)$ (the first column) and the corresponding translational correlation function (the second column in log-log scale and the third in log-linear scale) at the Bragg peaks \mathbf{q}_x , \mathbf{q}_y , and \mathbf{q}_t . In AD-I, the translational correlation function decays faster than power law along all the three wave vectors, indicating short-range translational orders. In AD-II, the system also exhibits short-range order along \mathbf{q}_y and \mathbf{q}_t , while it has a power-law decay along the $\hat{\mathbf{x}}$ axis indicating a QLR translational order.

In Figs. 6(a) and 6(b) we plot the correlation functions of the active force director $\langle \mathbf{n}(0) \cdot \mathbf{n}(\tilde{r}) \rangle_c$ of 10 independent samples (indicated by different colors). We find a power-law decay indicating QLRO of the active force directors in both AD-I and AD-II. Similarly, the velocity correlation functions $\langle \hat{v}(0) \cdot \hat{v}(\tilde{r}) \rangle_c$ as shown in Figs. 6(c) and 6(d) also exhibit

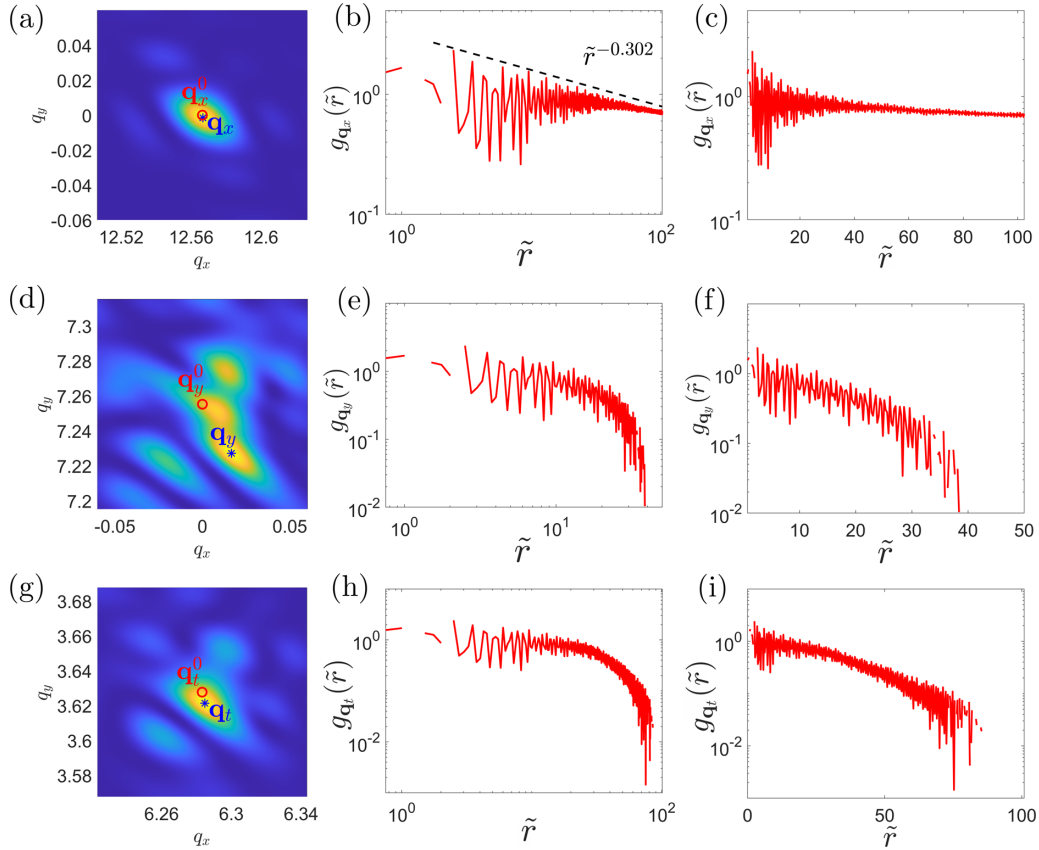


FIG. 5. Bragg peak of $Q(q_x, q_y)$ which are numerically evaluated (\mathbf{q}_x , \mathbf{q}_y , and \mathbf{q}_z) and that of a perfect hexagonal lattice (\mathbf{q}_x^0 , \mathbf{q}_y^0 , and \mathbf{q}_z^0), and the corresponding translational correlation function in AD-II with [(a)–(c)] $\mathbf{q}_x = (12.5667, -0.0015)$ and $\mathbf{q}_x^0 = (4\pi, 0)$; [(d)–(f)] $\mathbf{q}_y = (0.0166, 7.2272)$ and $\mathbf{q}_y^0 = (0, 2\pi/(\sqrt{3}/2))$; [(g)–(i)] $\mathbf{q}_z = (6.2847, 3.6213)$ and $\mathbf{q}_z^0 = 2\pi(1, 1/\sqrt{3})$. The second column is in log-log scale, while the third column is in log-linear scale.

power-law decay, which again indicates QLRO of the velocity field in both cases. Furthermore, a linear fitting to the average of the 10 independent sample curves all give a power-law exponent very close to unity.

In Figs. 6(e) and 6(f), we show that the bond-orientational correlation function $g_6(\tilde{r})$ has a power-law decay with a nonzero but small exponent -0.0284 in AD-I, while it converges to a finite limit at large distances for AD-II. Hence the bond orientational order is quasi-long ranged for AD-I and long ranged for AD-II.

In summary, the moving phase of AD-I exhibits QLRO in active force director, velocity, and bond orientation, but only has SR translational order. Hence it should be categorized as a *moving hexatic phase*. By contrast, the moving phase of AD-II exhibits QLRO in active force director and velocity and LRO in bond orientation, yet the translation order is quasi-long ranged along the moving direction and short ranged in the other directions. This resembles the active smectic phase [53,54], even though there is no visible layer structures in our system. These numerical results indicate that there is no enhancement of velocity order due to translational order. On the contrary, alignment interactions tend to destabilize translational order in active crystals and that the destabilizing effect is stronger for Vicsek-like alignment (AD-I) than for elasticity-based alignment (AD-II).

IV. ANALYTIC RESULTS

To obtain a more thorough understanding of the moving phase of active crystals, we study a continuum theory of active solid which is inspired by our simulation model. Although a systematic procedure of coarse-graining [55–57] may be applied on the simulation model to obtain the continuum theory, we shall be content with heuristic and informal derivations.

In the present case, the derivation of the continuum equations constitutes of three steps: (1) We replace the variables \mathbf{r}_i , θ_i , $\mathbf{n}(\theta_i)$, and $\xi_i(t)$ and associated parameters, which are defined on lattice points, by continuous fields $\mathbf{R}(\mathbf{r})$, $\theta(\mathbf{r})$, $\mathbf{n}(\theta(\mathbf{r}))$, and $\xi(\mathbf{r}, t)$ and parameters; (2) we replace the elastic force Eq. (2) acting on a swimmer by its counterpart from continuum elasticity theory; and, finally, (3) we Taylor expand the dynamical equations up to first order in θ and second order in derivatives.

Since we are interested in the moving phase, it is convenient to parametrize the instantaneous positions of swimmers in the laboratory frame as

$$\mathbf{R}(\mathbf{r}, t) \equiv \mathbf{r} + \mathbf{u}(\mathbf{r}, t) + \mathbf{v}_0 t, \quad (13)$$

where \mathbf{r} is the Lagrangian coordinate, \mathbf{v}_0 is the velocity of collective motion, and $\mathbf{u}(\mathbf{r}, t)$ is the displacement field defined relative to the undeformed uniformly moving state.

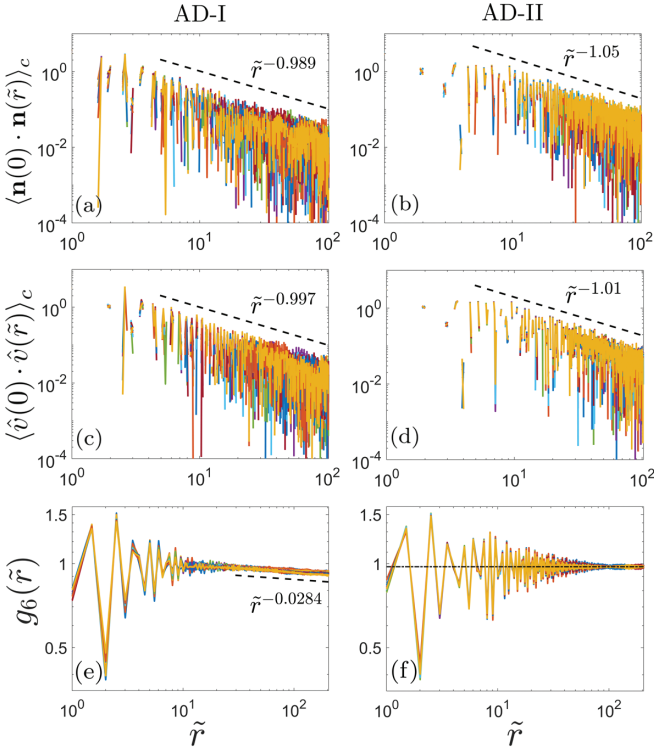


FIG. 6. [(a) and (b)] Correlation functions of the active force director \mathbf{n} , [(c) and (d)] correlation functions of velocity \hat{v} , and [(e) and (f)] the bond-orientational correlation functions $g_6(\tilde{r})$ of 10 independent samples at different simulation steps as indicated by different colors. Data are collected after the system reaches a steady state with $P \approx 0.9915$ in AD-I and $P \approx 0.9830$ in AD-II. The linear fitting at large \tilde{r} is applied to the average of the 10 sample curves. Left column: AD-I; right column: AD-II. The parameters are specified in the main text.

We assume that the system is moving along the $\hat{\mathbf{x}}$ axis and that the fluctuations of the director field away from the $\hat{\mathbf{x}}$ axis are small, such that $\mathbf{n}(\mathbf{r}, t) \approx \hat{\mathbf{x}} + \theta(\mathbf{r}, t)\hat{\mathbf{y}}$ with $\langle \theta(\mathbf{r}, t) \rangle = 0$ and $|\theta(\mathbf{r}, t)| \ll 1$. We substitute Eq. (13) back into Eq. (1) and find:

$$\gamma v_0 \hat{\mathbf{x}} + \gamma \dot{\mathbf{u}}(\mathbf{r}, t) \approx b \hat{\mathbf{x}} + b \theta(\mathbf{r}, t) \hat{\mathbf{y}} + \mathbf{F}(\mathbf{r}, t) + \gamma \sqrt{2D} \boldsymbol{\xi}(\mathbf{r}, t), \quad (14)$$

where γ , b , and D are the continuum counterpart of the parameters γ_p , b_p , and D_p in the particle model and $\boldsymbol{\xi}(\mathbf{r}, t)$ is a normalized two-dimensional Gaussian white noise:

$$\langle \xi_i(\mathbf{r}, t) \rangle = 0, \quad (15)$$

$$\langle \xi_i(\mathbf{r}, t) \xi_j(\mathbf{r}', t') \rangle = \delta_{ij} \delta(\mathbf{r} - \mathbf{r}') \delta(t - t'). \quad (16)$$

From this we immediately see that the collective moving velocity is $v_0 = b/\gamma$, and hence Eq. (14) becomes a stochastic

partial-differential equation (SPDE):

$$\gamma \dot{\mathbf{u}}(\mathbf{r}, t) = b \theta(\mathbf{r}, t) \hat{\mathbf{y}} + \mathbf{F}(\mathbf{r}, t) + \gamma \sqrt{2D} \boldsymbol{\xi}(\mathbf{r}, t), \quad (17)$$

A nonvanishing $\theta(\mathbf{r}, t)$ implies rotation of the active force away from the $\hat{\mathbf{x}}$ axis, which, according to Eq. (17), leads to a nonvanishing active force along the $\hat{\mathbf{y}}$ axis. This is, of course, obviously correct.

The elastic force in Eqs. (14) and (17) are described by linear isotropic elasticity theory [50,58,59]:

$$\mathbf{F} = \mu \nabla^2 \mathbf{u} + (\lambda + \mu) \nabla (\nabla \cdot \mathbf{u}), \quad (18a)$$

where λ and μ are two independent Lamé coefficients characterizing the solid elasticity. This is the continuum counterpart of \mathbf{F}_i in Eq. (2). In components we have

$$\begin{aligned} F_x &= (\lambda + 2\mu) \partial_x^2 u_x + \mu \partial_y^2 u_x + (\lambda + \mu) \partial_x \partial_y u_y, \\ F_y &= (\lambda + 2\mu) \partial_y^2 u_y + \mu \partial_x^2 u_y + (\lambda + \mu) \partial_x \partial_y u_x, \end{aligned} \quad (18b)$$

where $\lambda = \mu = \kappa \sqrt{3}/4$ for two-dimensional triangular lattice [60] with κ the elastic constant shown in Eq. (2). Note that the elasticity theory shown in Eq. (18a) is isotropic, and hence the direction of collective motion can be arbitrarily chosen. The choice of the direction of collective moving along $\hat{\mathbf{x}}$ axis does not lose generality for the continuum model.

A. Analytic results of AD-I

The derivation of the continuum dynamic equation for θ can be similarly carried out. For AD-I, the details and the result are explained in Appendix C. Combining with Eq. (17), we obtain for AD-I the following set of linearized SPDEs:

$$\begin{aligned} \gamma \dot{u}_x &= F_x + \gamma \sqrt{2D} \xi_x \\ \gamma \dot{u}_y &= b \theta + F_y + \gamma \sqrt{2D} \xi_y. \\ \dot{\theta} &= g \Delta \theta + \sqrt{2D} \eta \end{aligned} \quad (19)$$

where $\eta = \eta(\mathbf{r}, t)$ is a normalized Gaussian white noise with $\langle \eta(\mathbf{r}, t) \rangle = 0$, $\langle \eta(\mathbf{r}, t) \eta(\mathbf{r}', t') \rangle = \delta(\mathbf{r} - \mathbf{r}') \delta(t - t')$.

Following the method discussed in Appendix D, we implement a Fourier transform (FT) for the spatial coordinates of Eqs. (19) and obtain a Lyapunov equation:

$$\begin{pmatrix} \dot{\hat{u}}_x \\ \dot{\hat{u}}_y \\ \dot{\hat{\theta}} \end{pmatrix} + \boldsymbol{\Gamma} \begin{pmatrix} \hat{u}_x \\ \hat{u}_y \\ \hat{\theta} \end{pmatrix} = \begin{pmatrix} \sqrt{2D} \xi_x \\ \sqrt{2D} \xi_y \\ \sqrt{2D} \eta \end{pmatrix}, \quad (20)$$

where the matrix $\boldsymbol{\Gamma}$ is given by

$$\boldsymbol{\Gamma} = \frac{1}{\gamma} \begin{bmatrix} \lambda(3k_x^2 + k_y^2) & 2\lambda k_x k_y & 0 \\ 2\lambda k_x k_y & \lambda(3k_y^2 + k_x^2) & -b \\ 0 & 0 & \gamma g(k_x^2 + k_y^2) \end{bmatrix}. \quad (21)$$

We further define the diagonal noise matrix $\mathbf{B} = \text{diag}(D, D, D^\theta)$ and the correlation matrix:

$$\mathbf{M} = \begin{pmatrix} \langle |\hat{u}_x|^2 \rangle & \langle \hat{u}_x \hat{u}_y^* \rangle & \langle \hat{u}_x \hat{\theta}^* \rangle \\ \langle \hat{u}_y \hat{u}_x^* \rangle & \langle |\hat{u}_y|^2 \rangle & \langle \hat{u}_y \hat{\theta}^* \rangle \\ \langle \hat{\theta} \hat{u}_x^* \rangle & \langle \hat{\theta} \hat{u}_y^* \rangle & \langle |\hat{\theta}|^2 \rangle \end{pmatrix}. \quad (22)$$

The steady-state correlation functions for $\mathbf{u}(\mathbf{k}, t)$ and $\theta(\mathbf{k}, t)$ can then be obtained by solving Eq. (D6):

$$\langle |\hat{u}_x(\mathbf{k})|^2 \rangle = \frac{D(k_x^2 + 3k_y^2)\gamma}{3k^4\lambda} + \frac{b^2 D^\theta k_x^2 k_y^2 (\gamma + 4\lambda)}{3k^{10}\lambda g(g^2\gamma^2 + 4g\gamma\lambda + 3\lambda^2)} \equiv \frac{W_1(\alpha)}{k^6} + \frac{W_2(\alpha)}{k^2}, \quad (23a)$$

$$\langle |\hat{u}_y(\mathbf{k})|^2 \rangle = \frac{D(3k_x^2 + k_y^2)\gamma}{3k^4\lambda} + \frac{b^2 D^\theta [g(3k_x^4 + 3k_x^2 k_y^2 + k_y^4)\gamma + (3k_x^2 + k_y^2)^2 \lambda]}{3k^{10}\lambda g(g^2\gamma^2 + 4g\gamma\lambda + 3\lambda^2)} \equiv \frac{W_3(\alpha)}{k^6} + \frac{W_4(\alpha)}{k^2}, \quad (23b)$$

$$\langle |\hat{\theta}(\mathbf{k})|^2 \rangle = \frac{D^\theta}{gk^2}. \quad (23c)$$

where $k = |\mathbf{k}| = (k_x^2 + k_y^2)^{-1/2}$ and α is the polar angle of \mathbf{k} . The functions $W_i(\alpha)$ are defined as

$$W_1(\alpha) = \frac{b^2 D^\theta (g\gamma + 4\lambda) \sin^2 2\alpha}{12g\lambda(g^2\gamma^2 + 4g\gamma\lambda + 3\lambda^2)}, \quad W_2(\alpha) = \frac{\gamma D(2 - \cos 2\alpha)}{3\lambda}, \quad (24a)$$

$$W_3(\alpha) = \frac{b^2 D^\theta [g\gamma(15 + 8 \cos 2\alpha + \cos 4\alpha) + \lambda(36 + 32 \cos 2\alpha + 4 \cos 4\alpha)]}{24g\lambda(g^2\gamma^2 + 4g\gamma\lambda + 3\lambda^2)}, \quad (24b)$$

$$W_4(\alpha) = \frac{\gamma D(2 + \cos 2\alpha)}{3\lambda}. \quad (24c)$$

Various functions appearing in $W_i(\alpha)$ are plotted in Fig. 7. It can be seen there that $W_2(\alpha)$, $W_3(\alpha)$, and $W_4(\alpha)$ are all strictly positive, whereas $W_1(\alpha)$ is positive except along the \hat{k}_x and \hat{k}_y axes, where $\alpha = 0, \pi/2, \pi, 3\pi/2$, respectively. Hence only along these axes does $\langle |\hat{u}_x(\mathbf{k})|^2 \rangle$ scale as k^{-2} instead of k^{-6} along other directions.

The real space fluctuations of displacement fields and director field can be obtained by implementing inverse Fourier transform to Eqs. (23a), (23b), and (23c) over the \mathbf{k} space. Integrating Eqs. (23a) and (23b) we see that $\langle u_x(\mathbf{r}, t)^2 \rangle$ and $\langle u_y(\mathbf{r}, t)^2 \rangle$ diverge in power law with system size, indicating SR translation orders which agree with our numerical observations in Fig. 4. On the other hand, integrating Eq. (23c) we see that $\langle \theta(\mathbf{r}, t)^2 \rangle$ diverges logarithmically with system size, and hence the active force exhibits QLRO. Since the velocity is massively coupled to the active force, it should also exhibit QLRO, as demonstrated by our numerical simulation.

B. Analytic results of AD-II

For AD-II, the derivation of the dynamic equation for θ , Eq. (AD-II), is trivial: We only need to replace various variables and elastic force by their continuum counterparts, and

further expand the equation to first order in θ . The details and the result are also explained in Appendix C. The resulting dynamical equations are

$$\begin{aligned} \gamma \dot{u}_x &= F_x + \gamma \sqrt{2D} \xi_x, \\ \gamma \dot{u}_y &= b\theta + F_y + \gamma \sqrt{2D} \xi_y, \\ \dot{\theta} &= c F_y + \sqrt{2D^\theta} \eta. \end{aligned} \quad (25)$$

Again using the method in Appendix D, we implement the Fourier transform to the spatial coordinates and find:

$$\begin{pmatrix} \hat{u}_x \\ \hat{u}_y \\ \hat{\theta} \end{pmatrix} + \mathbf{\Gamma} \begin{pmatrix} \hat{u}_x \\ \hat{u}_y \\ \hat{\theta} \end{pmatrix} = \begin{pmatrix} \sqrt{2D} \xi_x \\ \sqrt{2D} \xi_y \\ \sqrt{2D^\theta} \eta \end{pmatrix}, \quad (26)$$

where the matrix \mathbf{B} and \mathbf{M} are the same as those in (AD-I) and $\mathbf{\Gamma}$ is given by

$$\mathbf{\Gamma} = \frac{1}{\gamma} \begin{pmatrix} \lambda(3k_x^2 + k_y^2) & 2\lambda k_x k_y & 0 \\ 2\lambda k_x k_y & \lambda(3k_y^2 + k_x^2) & -b \\ 2\gamma\lambda c k_x k_y & \gamma\lambda c(3k_y^2 + k_x^2) & 0 \end{pmatrix}. \quad (27)$$

The steady-state correlation functions for $\mathbf{u}(\mathbf{k}, t)$ and $\theta(\mathbf{k}, t)$ are then obtained in a similar way:

$$\langle |\hat{u}_x(\mathbf{k})|^2 \rangle = \frac{b[16D^\theta k_x^2 k_y^2 + c^2 D(k_x^4 + 12k_x^2 k_y^2 + 27k_y^4)\gamma^2] + 12cDk^4(k_x^2 + 3k_y^2)\gamma\lambda}{3ck^4\lambda[bc(k_x^2 + 9k_y^2)\gamma + 12k^4\lambda]} \quad (28a)$$

$$= \frac{W_5(\alpha)}{k^2} + \mathcal{O}(1), \text{ as } k \rightarrow 0, \quad (28b)$$

$$\langle |\hat{u}_y(\mathbf{k})|^2 \rangle = \frac{3b^2 c D^\theta k^2 \gamma + b(3k_x^2 + k_y^2)[4D^\theta(3k_x^2 + k_y^2) + c^2 D(k_x^2 + 9k_y^2)\gamma^2]\lambda + 12cDk^4(3k_x^2 + k_y^2)\gamma\lambda^2}{3ck^4\lambda^2[bc(k_x^2 + 9k_y^2)\gamma + 12k^4\lambda]} \quad (28c)$$

$$= \frac{W_6(\alpha)}{k^4} + \mathcal{O}\left(\frac{1}{k^2}\right), \text{ as } k \rightarrow 0, \quad (28d)$$

$$\langle |\hat{\theta}(\mathbf{k})|^2 \rangle = \frac{b^2 c^2 D^\theta (k_x^2 + 3k_y^2)\gamma^2 + bck^2\gamma[13D^\theta k^2 + c^2 D(k_x^2 + 9k_y^2)\gamma^2]\lambda + 12k^6(D^\theta + c^2\gamma^2 D)\lambda^2}{bck^2\lambda[bc(k_x^2 + 9k_y^2)\gamma + 12k^4\lambda]} \quad (28e)$$

$$= \frac{W_7(\alpha)}{k^2} + \mathcal{O}(1), \text{ as } k \rightarrow 0. \quad (28f)$$

where $W_5(\alpha)$, $W_6(\alpha)$, and $W_7(\alpha)$ are defined as

$$W_5(\alpha) = \frac{c^2\gamma^2 D(12 + 2\cos 4\alpha - 13\cos 2\alpha) + 2D^\theta(1 - \cos 4\alpha)}{3c^2\gamma\lambda(5 - 4\cos 2\alpha)}, \quad (29a)$$

$$W_6(\alpha) = \frac{bD^\theta}{c\lambda^2(5 - 4\cos 2\alpha)}, \quad W_7(\alpha) = \frac{\gamma D^\theta(2 - \cos 2\alpha)}{\lambda(5 - 4\cos 2\alpha)}. \quad (29b)$$

The functions appearing in $W_5(\alpha)$, $W_6(\alpha)$, and $W_7(\alpha)$ are also plotted in Fig. 7. It is obvious that $W_5(\alpha)$, $W_6(\alpha)$, and $W_7(\alpha)$ are all strictly positive. Implementing inverse Fourier transform to Eqs. (28b) and (28d), we see that translational order for AD-II is QLR along the $\hat{\mathbf{x}}$ axis and SR along the $\hat{\mathbf{y}}$ axis, consistent with the numerical results displayed in Fig. 5. Since Eq. (28f) scales the same as Eq. (23c), we see that the active force director order (as well as the velocity order) is also quasi-long ranged.

To make further comparison between the numerical and analytic results, we draw in Fig. 8 the contour plots of correlation functions $\langle |\hat{u}_x(\mathbf{k})|^2 \rangle$, $\langle |\hat{u}_y(\mathbf{k})|^2 \rangle$, and $\langle |\hat{\theta}(\mathbf{k})|^2 \rangle$ in the collective moving phase and find qualitative agreements between numerical and analytic results. The numerical results are shown in the first and third rows, whereas the analytical results are in the second and fourth rows. For dimensionless equations and parameters of the continuum model, see Appendix E.

We also plot in Fig. 9 the cut of $\langle |\hat{\theta}(\mathbf{k})|^2 \rangle$ along the positive \hat{k}_x axis and \hat{k}_y axis in \mathbf{k} space, observing a k^{-2} decay in AD-I and a k^{-2} decay followed by a constant in AD-II. These scaling properties match the analytical results along \hat{k}_x and \hat{k}_y of Eqn. (23c) for AD-I with the form $\langle |\hat{\theta}(k_x, 0)|^2 \rangle = D^\theta / (gk_x^2)$, $\langle |\hat{\theta}(k_y, 0)|^2 \rangle = D^\theta / (gk_y^2)$, and (28e) for AD-II with the form:

$$\langle |\hat{\theta}(k_x, 0)|^2 \rangle = \frac{\gamma D^\theta}{\lambda k_x^2} + \frac{D^\theta + c^2\gamma^2 D_T}{bc}, \quad (30)$$

$$\langle |\hat{\theta}(0, k_y)|^2 \rangle = \frac{\gamma D^\theta}{3\lambda k_y^2} + \frac{D^\theta + c^2\gamma^2 D_T}{bc}. \quad (31)$$

In the limit $b \rightarrow 0$, the \mathbf{u} correlations in both AD-I and AD-II, i.e., Eqs. (23a), (23b), (28a), and (28c), reduce exactly

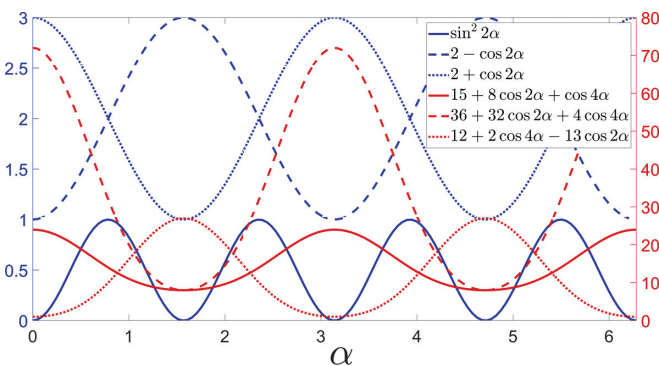


FIG. 7. Various functions appearing in $W_i(\alpha)$. It can be easily seen that all the terms are positive except $\sin^2 2\alpha$ at $\alpha = 0, \pi/2, \pi, 3\pi/2$. Since $W_1(\alpha)$ is proportional to $\sin^2 2\alpha$, it also vanishes in these places.

to those of passive crystals [50]:

$$\langle |\hat{u}_x(\mathbf{k})|^2 \rangle = \frac{\gamma D(2 - \cos 2\alpha)}{3\lambda k^2}, \quad (32)$$

$$\langle |\hat{u}_y(\mathbf{k})|^2 \rangle = \frac{\gamma D(2 + \cos 2\alpha)}{3\lambda k^2},$$

which further reduce to Eqs. (11) along \hat{k}_x and \hat{k}_y axes.

C. Generalization to higher dimensions

To achieve more thorough understanding of our models of active solids in the moving phase, we shall generalize the analytical theory to arbitrary spatial dimensions $d > 2$. For a pedagogical discussion of d -dimensional elasticity theory of isotropic solid, see Ref. [50]. The elastic force of a d -dimensional isotropic solid can be obtained by generalization of Eqs. (18). In fact, Eq. (18a) remains valid if we understand ∇ and \mathbf{u} as d -dimensional gradient operator and displacement field. In components we have

$$F_i = \mu \sum_{j=1}^d \partial_j^2 u_i + (\lambda + \mu) \sum_{j=1}^d \partial_i \partial_j u_j. \quad (33)$$

More specifically, for the 3D case, we have

$$F_x = \mu(\partial_x^2 u_x + \partial_y^2 u_x + \partial_z^2 u_x) + (\lambda + \mu)(\partial_x^2 u_x + \partial_x \partial_y u_y + \partial_x \partial_z u_z),$$

$$F_y = \mu(\partial_x^2 u_y + \partial_y^2 u_y + \partial_z^2 u_y) + (\lambda + \mu)(\partial_y \partial_x u_x + \partial_y^2 u_y + \partial_y \partial_z u_z),$$

$$F_z = \mu(\partial_x^2 u_z + \partial_y^2 u_z + \partial_z^2 u_z) + (\lambda + \mu)(\partial_z \partial_x u_x + \partial_z \partial_y u_y + \partial_z^2 u_z). \quad (34)$$

As before we shall choose the positive $\hat{\mathbf{x}}$ axis to be the direction of collective motion. It is then convenient to decompose \mathbf{u} and ∇ into $\mathbf{u} = (u_x, \mathbf{u}_\perp)$ and $\nabla = (\partial_x, \nabla_\perp)$, where \mathbf{u}_\perp and ∇_\perp denote respectively the $(d-1)$ -dimensional gradient operator and displacement field in the perpendicular subspace. The director field can be decomposed as $\mathbf{n} = (1, \delta\mathbf{n}_\perp)$, where again we have assumed that $|\delta\mathbf{n}_\perp| \ll 1$. The elastic force can be similarly decomposed, $\mathbf{F} = (F_x, \mathbf{F}_\perp)$, and each component is given by

$$F_x = \mu \nabla^2 u_x + (\lambda + \mu) \partial_x (\nabla \cdot \mathbf{u}), \quad (35a)$$

$$\mathbf{F}_\perp = \mu \nabla^2 \mathbf{u}_\perp + (\lambda + \mu) \nabla_\perp (\nabla \cdot \mathbf{u}). \quad (35b)$$

The overdamped dynamics of \mathbf{u} in the moving phase is then given by

$$\gamma \dot{\mathbf{u}}(\mathbf{r}, t) = b\mathbf{n}_\perp + \mathbf{F}(\mathbf{r}, t) + \gamma \sqrt{2D} \boldsymbol{\xi}(\mathbf{r}, t). \quad (36)$$

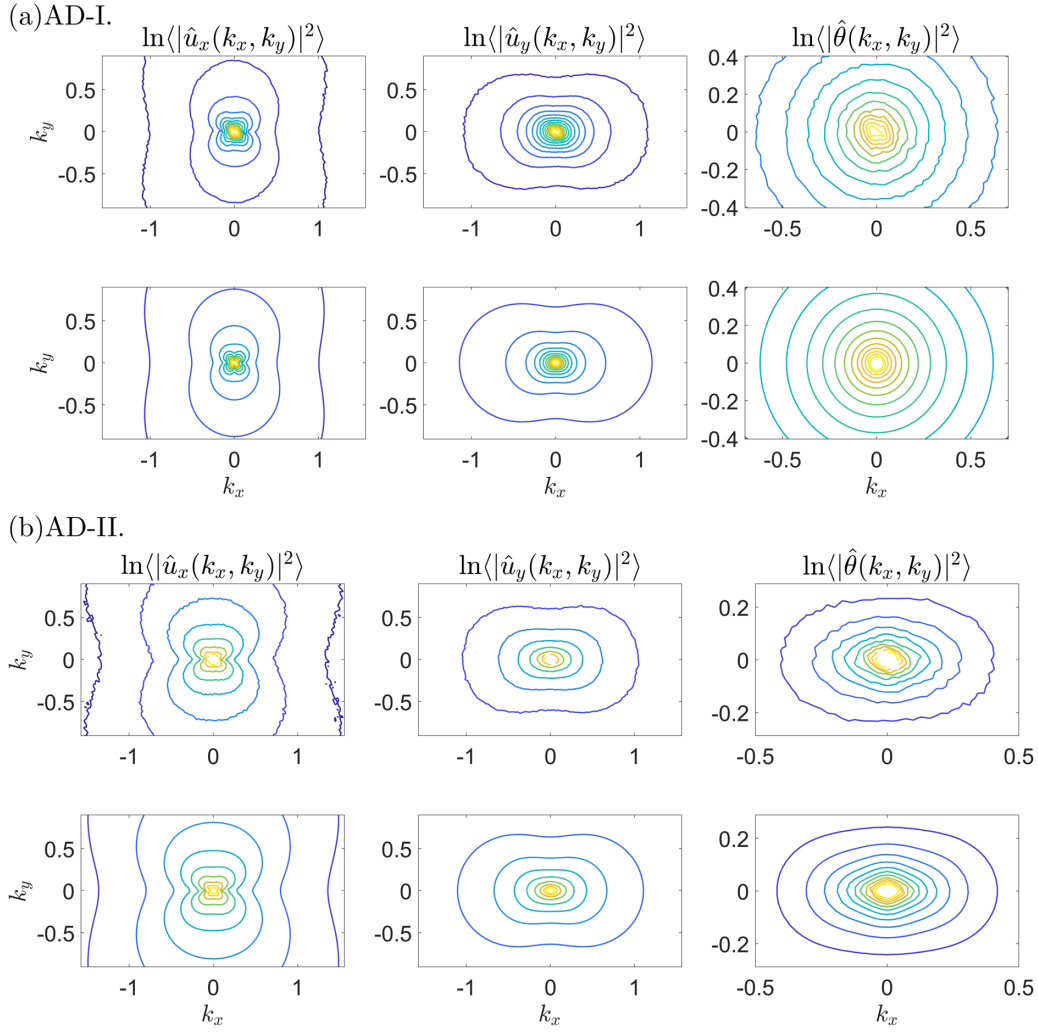


FIG. 8. Contour plot of the logarithm of the \mathbf{u} correlations $\langle |\hat{u}_x|^2 \rangle$, $\langle |\hat{u}_y|^2 \rangle$, and $\langle |\hat{\theta}|^2 \rangle$ in \mathbf{k} space in the collective moving phase for (a) AD-I and (b) AD-II. The first and third rows are results from simulations, whereas the second and fourth rows are results from analytic models.

where $\xi(\mathbf{r}, t) = \xi_x \hat{\mathbf{x}} + \xi_\perp$ is a d -dimensional Gaussian white noise. The dynamics of \mathbf{n}_\perp can be analogously obtained:

$$\dot{\mathbf{n}}_\perp(\mathbf{r}, t) = d \Delta \mathbf{n}_\perp + \sqrt{2D^\theta} \boldsymbol{\eta}_\perp(\mathbf{r}, t), \quad (\text{AD-I}')$$

$$\begin{aligned} \dot{\mathbf{n}}_\perp(\mathbf{r}, t) &= c (\mathbf{n} \times \mathbf{F}) \times \mathbf{n} + \sqrt{2D^\theta} \boldsymbol{\eta}_\perp(\mathbf{r}, t) \\ &= c \mathbf{F}_\perp + \sqrt{2D^\theta} \boldsymbol{\eta}_\perp(\mathbf{r}, t). \end{aligned} \quad (\text{AD-II}')$$

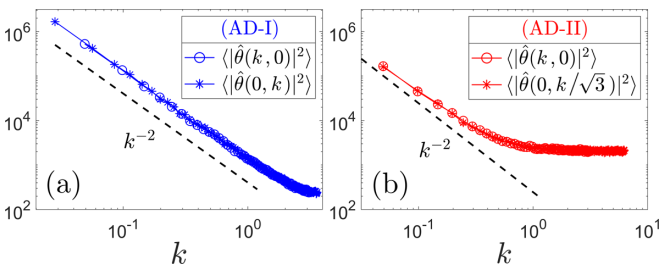


FIG. 9. The cut of $\langle |\hat{\theta}|^2 \rangle$ along the positive \hat{k}_x axis and \hat{k}_y axis in \mathbf{k} space. In AD-I, we observe a k^{-2} decay along both directions, while in AD-II both of the two k^{-2} scaling curves are followed by a constant term.

We can substitute Eq. (35) into Eq. (36) together with Eqs. (AD-I') and AD-II') and obtain the d -dimensional dynamical equations for AD-I and AD-II. For AD-I we have

$$\begin{aligned} \gamma \dot{u}_x &= F_x + \gamma \sqrt{2D} \xi_x \\ \gamma \dot{\mathbf{u}}_\perp &= b \mathbf{n}_\perp + \mathbf{F}_\perp + \gamma \sqrt{2D} \boldsymbol{\xi}_\perp \\ \dot{\mathbf{n}}_\perp &= d \Delta \mathbf{n}_\perp + \sqrt{2D^\theta} \boldsymbol{\eta}_\perp. \end{aligned} \quad (37)$$

For AD-II we have

$$\begin{aligned} \gamma \dot{u}_x &= F_x + \gamma \sqrt{2D} \xi_x \\ \gamma \dot{\mathbf{u}}_\perp &= b \mathbf{n}_\perp + \mathbf{F}_\perp + \gamma \sqrt{2D} \boldsymbol{\xi}_\perp \\ \dot{\mathbf{n}}_\perp &= c \mathbf{F}_\perp + \sqrt{2D^\theta} \boldsymbol{\eta}_\perp. \end{aligned} \quad (38)$$

It can be easily seen that Eqs. (37) and (38) have exactly the same structure as Eqs. (19) and (25). The correlation functions of \mathbf{u} field and \mathbf{n}_\perp field can be calculated using the same method, and the results have exactly the same structure as Eqs. (23) and (28), as long as we replace θ by \mathbf{n}_\perp .

We can now deduce the stability of director order and translational order by evaluating the real space fluctuations of the director field and the displacement field. For both AD-I

TABLE I. Stability of the translational order, bond-orientational order, active force director order, and velocity order of active crystals in 2D and 3D. In the stationary phase, bond-orientational order is always long ranged, whereas active force director is always short ranged.

		Stationary phase		Moving phase			
		\mathbf{u}	ψ_6	\mathbf{u}_{\parallel}	\mathbf{u}_{\perp}	\mathbf{n} & \hat{v}	ψ_6
2D	AD-I	QLRO	LRO	SRO	SRO	QLRO	QLRO
	AD-II	QLRO	LRO	QLRO	SRO	QLRO	LRO
3D	AD-I	LRO	LRO	SRO	SRO	LRO	LRO
	AD-II	LRO	LRO	LRO	SRO	LRO	LRO

and AD-II, correlation of \mathbf{n}_{\perp} scales as k^{-2} for small \mathbf{k} . This allows us to calculate \mathbf{n}_{\perp} fluctuations in real space:

$$\langle \mathbf{n}_{\perp}(\mathbf{r})^2 \rangle = \int d^d \mathbf{k} \langle \mathbf{n}_{\perp}(\mathbf{k})^2 \rangle \sim \int_{2\pi/L}^{2\pi/a_0} \frac{d^d \mathbf{k}}{k^2}, \quad (39)$$

where $2\pi/L$ is the low momentum cutoff set by the system size L and $2\pi/a_0$ is the high momentum cutoff set by lattice spacing. This integral diverges with system size for $d \leq 2$, which means that the lower critical dimension for director is $d_c^v = 2$. Similarly, Eqs. (23) show that the \mathbf{u} correlation for AD-I is k^{-6} , except on four discrete directions [the narrow regions where $W_1(\alpha)$ are vanishingly small do not affect the estimate of the divergence below]. The real space fluctuations of displacement field \mathbf{u}_{\perp} , u_x are then

$$\langle \mathbf{u}(\mathbf{r})^2 \rangle = \int d^d \mathbf{k} \langle \mathbf{u}(\mathbf{k})^2 \rangle \sim \int_{2\pi/L}^{2\pi/a_0} \frac{d^d \mathbf{k}}{k^6}, \quad (40)$$

which diverges with L for $d \leq 6$. Hence the lower critical dimension for translational order for AD-I is $d_c^t = 6$. Finally, Eqs. (28) show that correlation function of \mathbf{u}_{\perp} (displacement in transverse direction) scales as k^{-4} , whereas that of u_x (displacement in parallel direction) scales as k^{-2} . A similar calculation then shows that the lower critical dimension of translational order is $d_c^{\perp} = 4$ in perpendicular direction and $d_c^{\parallel} = 2$ in the parallel direction. The nature of various orders for the 2D and 3D cases are summarized in Table I. The nature of bond-orientational order, however, cannot be easily determined from our analytic theory. Nonetheless, given our 2D results, we deduce that the bond orientational order is long ranged above two dimensions both for AD-I and AD-II.

D. Validity of the linearization of θ

We have assumed that $|\theta| \ll 1$ in the theoretical analysis as well as in the simulation, under the choice of collective moving along the $\hat{\mathbf{x}}$ axis. In our simulation, the fluctuation of θ is indeed very weak, being of the order of 1/10 radian. Hence the linearization of θ is well justified.

For system with infinite system size, the real space fluctuations of θ and \mathbf{u} indeed diverge both for AD-I and for AD-II, as is demonstrated by our continuum theory. This implies that we need to study possible topological defects of active director, just as in classical equilibrium XY model. Is there a defects-unbinding transition similar to the Kosterlitz-Thouless

(KT) transition [61] in equilibrium 2D XY model? Does solid elasticity play an essential role and change the physics of KT transition? These questions are certainly interesting but can only be addressed by future studies.

V. CONCLUSION

In this work, we have provided a complete characterization of various orders in two different models of active solids. These results may be readily checked by future experiments of active systems. It would also be interesting to study whether the phases we discovered are related to those solidlike moving structures observed in Vicsek-type models with short-range interactions [21,22].

ACKNOWLEDGMENTS

X.X. acknowledge support from NSFC via Grant No. 11674217, as well as additional support from a Shanghai Talent Program. This research is also supported by Shanghai Municipal Science and Technology Major Project (Grant No. 2019SHZDZX01).

APPENDIX A: NUMERICAL INTEGRATOR

In this Appendix, we present the discretized dynamical equations for $\tilde{\mathbf{r}}$ and θ , obtained by applying the first-order Euler-Maruyama scheme [48] to Eqs. (4) and (AD- $\tilde{\mathbf{I}}$) or (AD- $\tilde{\mathbf{II}}$) in the main text. The equation for $\tilde{\mathbf{r}}$ is

$$\dot{\tilde{\mathbf{r}}}_i(\tilde{t} + \Delta\tilde{t}) = \dot{\tilde{\mathbf{r}}}_i(\tilde{t}) + \Delta\tilde{t}[\tilde{b}_p \mathbf{n}(\theta_i(\tilde{t})) + \tilde{\mathbf{F}}_i(\tilde{t})] + \mathbf{V} \sqrt{2\tilde{D}_p \Delta\tilde{t}}. \quad (A1)$$

The equations of θ for AD-I or AD-II are respectively:

$$\begin{aligned} \dot{\theta}_i(\tilde{t} + \Delta\tilde{t}) = & \dot{\theta}_i(\tilde{t}) + \Delta\tilde{t}[\tilde{d}_p(\mathbf{n}(\theta_i(\tilde{t})) \\ & \times \langle \mathbf{n} \rangle_i) \cdot \hat{\mathbf{z}}] + W \sqrt{2\tilde{D}_p^\theta \Delta\tilde{t}}, \end{aligned} \quad (A2)$$

$$\begin{aligned} \dot{\theta}_i(\tilde{t} + \Delta\tilde{t}) = & \dot{\theta}_i(\tilde{t}) + \Delta\tilde{t}[\tilde{c}_p(\mathbf{n}(\theta_i(\tilde{t})) \times \tilde{\mathbf{F}}_i) \cdot \hat{\mathbf{z}}] \\ & + W \sqrt{2\tilde{D}_p^\theta \Delta\tilde{t}}. \end{aligned} \quad (A3)$$

where \mathbf{V} and W are normalized two- and one-dimensional Gaussian variables, respectively. The time step is chosen as $\Delta\tilde{t} = 10^{-3}$.

APPENDIX B: FOURIER TRANSFORM ON TRIANGULAR LATTICE

For brevity and clarity, we omit the tilde symbol for the dimensionless variables in this section, keeping in mind that the quantities all refer to their dimensionless counterparts when we apply the technique in our simulations.

The simulations use a triangular lattice with a rhomblike boundary, where the lattice points are shown in Fig. 10 as the solid black points. We wish to implement the FT to the data (e.g., the displacement u_x , u_y , and the angle θ) sampled on this triangular lattice into the reciprocal \mathbf{k} space. Although it is easy to implement FT on a square lattice by using the fast Fourier transform (FFT) techniques, no direct method exists for FT on a triangular lattice. However, the triangular lattice

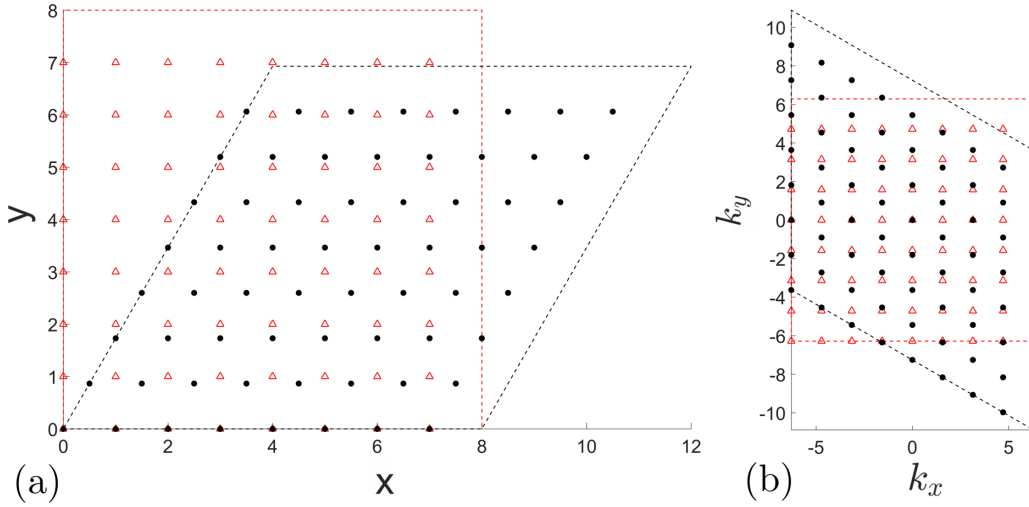


FIG. 10. A lattice with lattice constant $a_0 = 1$ and $L = 8$. The black points denote (a) sample points in real space and (b) the corresponding \mathbf{k} -space points. The red triangles are the standard grid in each space, respectively. The black dashed lines in (a) denote the boundary of the simulation box.

can be deemed as originating from a linear transform of the square lattice. Since FT is also a linear transform, we expect a combination of the two linear transforms may serve our purpose. Below is a derivation of this process.

Suppose we sample a complex function $f : \mathbb{R}^n \rightarrow \mathbb{C}$ on a set of n -dimensional points $\Lambda \in \mathbb{R}^n$ in real space. Let $\Phi : \mathbb{R}^n \rightarrow \mathbb{R}^n$ be a linear isomorphic map under which n -dimensional integers are mapped to n -dimensional real values such that $\mathbb{Z}^n \rightarrow \Lambda$. We may obtain the FT of f in terms of the FT of $(f \circ \Phi)$, which is a function on \mathbb{Z}^n . The FT of $(f \circ \Phi)$ is

$$\begin{aligned} \mathcal{F}(f \circ \Phi)(s) &\equiv \int f \circ \Phi(x) e^{-2\pi i(s,x)} dx \\ &= \frac{1}{|\det \Phi|} \int f(y) e^{-2\pi i(\Phi^{-T}s,y)} dy \\ &= \frac{1}{|\det \Phi|} \mathcal{F}(f)(\Phi^{-T}s). \end{aligned} \quad (\text{B1})$$

Here a substitution $y = \Phi x$ was made, and it was used that $\langle s, \Phi^{-1}y \rangle = \langle \Phi^{-T}s, y \rangle$. Note that the conventions with respect to the sign of the exponent and factors of 2π may differ.

We now discuss the meaning of the above formula. The function $f \circ \Phi$ is the value of the sample points of f arranged in an n -dimensional array lying on a *standard grid* (equal-axis orthogonal grid). Its Fourier transform gives an array of the same shape, but the interpretation is different: The value at index s in reality is the value at $\Phi^{-T}s \in \mathbb{R}^n$ in k space, differing by a multiplier $|\det \Phi|$.

In our simulation's setup, the space dimension $n = 2$ and $\Lambda \in \mathbb{R}^2$ is the set of the triangular lattice points in real space. The function f whose FT we want to compute can be the displacement field u_x, u_y or the orientation field θ . The linear map $\mathbf{y} = \Phi \mathbf{x}$ with $\Phi = \begin{pmatrix} 1 & \frac{1}{\sqrt{3}} \\ 0 & \frac{2}{\sqrt{3}} \end{pmatrix}$ transforms a square regular lattice with lattice constant a_0 into the desired triangular lattice with the same lattice constant. The transverse of its inverse is $\Phi^{-T} = \begin{pmatrix} \frac{1}{\sqrt{3}} & 0 \\ -\frac{1}{3} & \frac{2}{3} \end{pmatrix}$. The function $f \circ \Phi$ takes the

value of the sample points of f on Λ , but its arguments lie on the corresponding square lattice points. We apply FFT on this real-space square lattice (standard grid), obtain its FT values on a \mathbf{k} -space square lattice (standard grid) indexed by s , and assign the FT values to its true coordinate in \mathbf{k} space by left multiplying Φ^{-T} to s . Suppose the standard grid in real space has a linear size $L \times L$ and each dimension is divided into equally spaced n points with distance of unity $a_0 = 1$; then there are $n \times n$ total sample points in both real and \mathbf{k} space.

In Fig. 10, a lattice of $L = 8$ and $n = 8$ is shown. The lattice constant of the standard grid in real space is $a_0 = 1$ and that in \mathbf{k} space is $\Delta k = 2\pi/L = \pi/4$. The \mathbf{k} -space vector of the standard grid with the minimal magnitude $\mathbf{s}_1 = (0, \frac{2\pi}{L})$ transforms to the true \mathbf{k} -space coordinate, $\mathbf{g}_1 = (0, \frac{2\pi}{L} \frac{2}{\sqrt{3}})$, while $\mathbf{s}_2 = (\frac{2\pi}{L}, 0)$ transforms to $\mathbf{g}_2 = (\frac{2\pi}{L}, -\frac{1}{\sqrt{3}} \frac{2\pi}{L})$ with both $|\mathbf{g}_i| = \frac{2\pi}{L} \frac{2}{\sqrt{3}}$.

APPENDIX C: CONTINUUM DESCRIPTION OF θ ALIGNMENT DYNAMICS

In this Appendix, we heuristically derive a continuum description of θ alignment dynamics for both AD-I and AD-II.

Similarly to the discussion at the beginning of Sec. IV for \mathbf{u} , the derivation of the continuum equations for θ dynamics in AD-I and AD-II constitutes the following steps: (1) We replace the variables θ_i , $\mathbf{n}(\theta_i)$, and $\eta_i(t)$ and associated parameters g_p , c_p , and D_p^θ , which are defined on lattice points, by continuous fields $\theta(\mathbf{r})$, $\mathbf{n}(\theta(\mathbf{r}))$, and $\eta(\mathbf{r}, t)$ and parameters g, c , and D^θ and (2) we Taylor expand the alignment terms up to first order in θ and second order in derivatives.

We first derive the continuous form of the alignment term $\mathbf{n}(\theta_i) \times (\mathbf{n}_i)_i \cdot \hat{\mathbf{z}}$ in Eq. (AD-I) of Sec. II into its counterpart $\Delta\theta$ in Eq. (19) of Sec. IV A. Assuming that the director $\mathbf{n}(\theta_i)$ changes slowly in space and can be described by a continuous unit vector field $\mathbf{n}(x, y)$, such that for dx, dy of the order of lattice spacing a_0 , the vector field near the position (x, y) can be well approximated by its Taylor expansion to the

second order:

$$\mathbf{n}(x + dx, y + dy) \approx \mathbf{n}(x, y) + (dx\partial_x + dy\partial_y)\mathbf{n}(x, y) + \frac{1}{2}(dx\partial_x + dy\partial_y)^2\mathbf{n}(x, y). \quad (\text{C1})$$

For a given lattice point, its six nearest neighbors are given by

$$(dx, dy) = (\pm a_0, 0), (\pm a_0/2, \pm\sqrt{3}a_0/2). \quad (\text{C2})$$

The average active director of the six neighbors, after combining like terms, is

$$\begin{aligned} \langle \mathbf{n} \rangle_i &\equiv \sum_{j \text{ n.n. } i} \mathbf{n}(\theta_j)/6 \approx \mathbf{n}(\theta_i) + \frac{a_0^2}{4}(\partial_y^2 + \partial_x^2)\mathbf{n}(\theta_i) \\ &= \mathbf{n}(\theta_i) + \frac{a_0^2}{4}\Delta\mathbf{n}(\theta_i). \end{aligned} \quad (\text{C3})$$

Substituting Eq. (C3) into the term $(\mathbf{n}(\theta_i) \times \langle \mathbf{n} \rangle_i) \cdot \hat{\mathbf{z}}$ in Eq. (AD-I), we obtain:

$$\begin{aligned} (\mathbf{n}(\theta_i) \times \langle \mathbf{n} \rangle_i) \cdot \hat{\mathbf{z}} &= \cos\theta_i \left(\sin\theta_i + \frac{a_0^2}{4}\Delta\sin\theta_i \right) \\ &\quad - \sin\theta_i \left(\cos\theta_i + \frac{a_0^2}{4}\Delta\cos\theta_i \right) \\ &= \frac{a_0^2}{4}\Delta\theta. \end{aligned} \quad (\text{C4})$$

This builds up the correspondence between $(\mathbf{n}(\theta_i) \times \langle \mathbf{n} \rangle_i) \cdot \hat{\mathbf{z}}$ in Eq. (AD-I) of the particle model and its counterpart $\Delta\theta$ in Eq. (19) of the continuum model. Omitting the coefficients in

Eq. (C4), the θ dynamics of AD-I in the continuum model is

$$\dot{\theta} = g\Delta\theta + \sqrt{2D^\theta}\eta, \quad (\text{C5})$$

as given in Eq. (19).

The treatment for the θ dynamics of AD-II is similar: Decompose the elastic force as $\mathbf{F} = (F_x, F_y)$ and then put it into the continuous version of Eq. (AD-II) together with the assumption $\mathbf{n}(\mathbf{r}, t) \approx \hat{\mathbf{x}} + \theta(\mathbf{r}, t)\hat{\mathbf{y}}$ and keep only the leading term, and the alignment term $(\mathbf{n}(\theta) \times \mathbf{F}) \cdot \hat{\mathbf{z}}$ becomes F_y . Then we have the θ dynamics in the continuum model of AD-II:

$$\dot{\theta} = cF_y + \sqrt{2D^\theta}\eta, \quad (\text{C6})$$

as given in Eq. (25).

APPENDIX D: CALCULATING CORRELATION FUNCTIONS

Here we discuss a general method for finding steady-state correlation of general multidimensional Langevin equations:

$$\dot{\mathbf{x}}(\mathbf{k}, t) + \mathbf{\Gamma}\mathbf{x}(\mathbf{k}, t) = \boldsymbol{\zeta}(\mathbf{k}, t), \quad (\text{D1})$$

where $\langle \zeta_i(\mathbf{k}, t)\zeta_j^T(\mathbf{k}', t') \rangle = \langle \zeta_i(\mathbf{k}, t)\zeta_j(-\mathbf{k}', t') \rangle = 2B_{ij}\delta(\mathbf{k} - \mathbf{k}')\delta(t - t')$. The matrices \mathbf{B} and $\mathbf{\Gamma}$ are assumed to be real, and $\mathbf{x}(\mathbf{k}, t)$ and $\boldsymbol{\zeta}(\mathbf{k}, t)$ are column vectors. Defining $\mathbf{y} = e^{\mathbf{\Gamma}t}\mathbf{x}$, it is easy to prove $d\mathbf{y}/dt = e^{\mathbf{\Gamma}t}\boldsymbol{\zeta}$, and we have the formal solution:

$$\mathbf{x}(\mathbf{k}, t) = \int_{-\infty}^t e^{-\mathbf{\Gamma}(t-\tau)}\boldsymbol{\zeta}(\mathbf{k}, \tau)d\tau. \quad (\text{D2})$$

The correlation matrix is

$$\begin{aligned} \langle \mathbf{x}(\mathbf{k}, t)\mathbf{x}^T(\mathbf{k}', t') \rangle &= \int_{-\infty}^t \int_{-\infty}^{t'} e^{-\mathbf{\Gamma}(t-\tau)} 2\mathbf{B}\delta(\mathbf{k} - \mathbf{k}')\delta(\tau - \tau') e^{-\mathbf{\Gamma}^T(t'-\tau')} d\tau d\tau' \\ &= \int_{-\infty}^{\min(t, t')} e^{-\mathbf{\Gamma}(t-\tau)} 2\mathbf{B}\delta(\mathbf{k} - \mathbf{k}') e^{-\mathbf{\Gamma}^T(t'-\tau)} d\tau. \end{aligned} \quad (\text{D3})$$

Defining the autocorrelation matrix $\mathbf{M}(\mathbf{k}, t) \equiv \mathbf{M}$ as

$$\mathbf{M} = \int \langle \mathbf{x}(\mathbf{k}, t)\mathbf{x}^T(\mathbf{k}', t) \rangle d\mathbf{k}' = \int_{-\infty}^t e^{-\mathbf{\Gamma}(t-\tau)} 2\mathbf{B}e^{-\mathbf{\Gamma}^T(t-\tau)} d\tau, \quad (\text{D4})$$

we have

$$\mathbf{\Gamma}\mathbf{M} + \mathbf{M}\mathbf{\Gamma}^T = \int_{-\infty}^t e^{-\mathbf{\Gamma}(t-\tau)} 2(\mathbf{\Gamma}\mathbf{B} + \mathbf{B}\mathbf{\Gamma}^T) e^{-\mathbf{\Gamma}^T(t-\tau)} d\tau = 2e^{-\mathbf{\Gamma}t} \left[\int_{-\infty}^t \frac{d}{d\tau} (e^{\mathbf{\Gamma}\tau}\mathbf{B}e^{\mathbf{\Gamma}^T\tau}) d\tau \right] e^{-\mathbf{\Gamma}t} = 2\mathbf{B}. \quad (\text{D5})$$

Hence we have

$$\mathbf{\Gamma}\mathbf{M} + \mathbf{M}\mathbf{\Gamma}^T = 2\mathbf{B}, \quad (\text{D6})$$

which can be used to find the autocorrelation matrix \mathbf{M} in terms of $\mathbf{\Gamma}$ and \mathbf{B} . Equation (D6) is known as the *Lyapunov equation* [62].

APPENDIX E: DIMENSIONLESS FORMS OF THE CONTINUUM MODEL

Here we derive the dimensionless forms of the continuum model. Using the space and time units a_0 and τ_0 , we define the

reduced quantities:

$$\begin{aligned} \tilde{b} &\equiv \frac{b\tau_0}{\gamma a_0}, \quad \tilde{\mathbf{F}} \equiv \frac{\mathbf{F}\tau_0}{\gamma a_0}, \quad \begin{pmatrix} \tilde{\mu} \\ \tilde{\lambda} \end{pmatrix} \equiv \frac{\tau_0}{\gamma a_0^2} \begin{pmatrix} \mu \\ \lambda \end{pmatrix}, \\ \tilde{D} &\equiv \frac{D\tau_0}{a_0^2}, \quad \tilde{D}^\theta \equiv D^\theta\tau_0, \quad \tilde{\mathbf{u}} \equiv \mathbf{u}/a_0, \\ \tilde{d} &\equiv \frac{d\tau_0}{a_0^2}, \quad \tilde{c} \equiv c\gamma a_0, \quad \begin{pmatrix} \tilde{\eta} \\ \tilde{\xi} \end{pmatrix} \equiv \sqrt{\tau_0} \begin{pmatrix} \eta \\ \xi \end{pmatrix}. \end{aligned} \quad (\text{E1})$$

Equations (19) and (25) can then be rewritten into the following dimensionless forms:

$$\tilde{\mathbf{u}}(\tilde{\mathbf{r}}, \tilde{t}) = \tilde{b}\tilde{\theta}\hat{\mathbf{y}} + \tilde{\mathbf{F}}(\tilde{\mathbf{r}}, \tilde{t}) + \sqrt{2\tilde{D}}\tilde{\boldsymbol{\xi}}(\tilde{\mathbf{r}}, \tilde{t}), \quad (\text{E2})$$

$$\dot{\theta}(\tilde{\mathbf{r}}, \tilde{t}) = \tilde{d}\tilde{\Delta}\theta + \sqrt{2\tilde{D}^\theta}\tilde{\eta}(\tilde{\mathbf{r}}, \tilde{t}), \quad (\text{AD-I}')$$

$$\dot{\theta}(\tilde{\mathbf{r}}, \tilde{t}) = \tilde{c}(\mathbf{n} \times \tilde{\mathbf{F}}) \cdot \hat{\mathbf{z}} + \sqrt{2\tilde{D}^\theta}\tilde{\eta}(\tilde{\mathbf{r}}, \tilde{t}), \quad (\text{AD-II}')$$

where $\tilde{\Delta} \equiv a_0^2\Delta$. Since the Lamé coefficients of a triangular lattice are equivalent and can be related to the elastic constant via $\tilde{\lambda} = \tilde{\mu} = \tilde{\kappa}\sqrt{3}/4$ [60], we also apply this relation in the

continuous model in order to compare the two models. For a qualitative comparison with the particle model in Fig. 8, the other parameters are chosen as $\tilde{g}_p = \tilde{g} = 10$ and $\tilde{\kappa} = 100$ for AD-I, $\tilde{c}_p = \tilde{c} = 1$ and $\tilde{\kappa} = 20$ for AD-II, and $\tilde{b}_p = \tilde{b} = 2$, $\tilde{D}_p = \tilde{D} = 0.01$, and $\tilde{D}_p^\theta = \tilde{D}^\theta = 0.05$. These parameters are put into Eqs. (23) and (28) to compute the correlation functions.

-
- [1] J. Toner, Y. Tu, and S. Ramaswamy, Hydrodynamics and phases of flocks, *Ann. Phys.* **318**, 170 (2005).
- [2] S. Ramaswamy, The mechanics and statistics of active matter, *Annu. Rev. Condens. Matter Phys.* **1**, 323 (2010).
- [3] T. Vicsek and A. Zafeiris, Collective motion, *Phys. Rep.* **517**, 71 (2012).
- [4] M. C. Marchetti, J.-F. Joanny, S. Ramaswamy, T. B. Liverpool, J. Prost, M. Rao, and R. A. Simha, Hydrodynamics of soft active matter, *Rev. Mod. Phys.* **85**, 1143 (2013).
- [5] F. Ginelli, The physics of the vicsek model, *Eur. Phys. J.: Spec. Top.* **225**, 2099 (2016).
- [6] H. Chaté, Dry aligning dilute active matter, *Annu. Rev. Condens. Matter Phys.* **11**, 189 (2020).
- [7] N. D. Mermin and H. Wagner, Absence of Ferromagnetism or Antiferromagnetism in One-or Two-Dimensional Isotropic Heisenberg Models, *Phys. Rev. Lett.* **17**, 1133 (1966).
- [8] T. Vicsek, A. Czirók, E. Ben-Jacob, I. Cohen, and O. Shochet, Novel Type of Phase Transition in a System of Self-Driven Particles, *Phys. Rev. Lett.* **75**, 1226 (1995).
- [9] J. Toner and Y. Tu, Long-Range Order in a Two-Dimensional Dynamical XY Model: How Birds Fly Together, *Phys. Rev. Lett.* **75**, 4326 (1995).
- [10] J. Toner, Reanalysis of the hydrodynamic theory of fluid, polar-ordered flocks, *Phys. Rev. E* **86**, 031918 (2012).
- [11] Y. Tu, J. Toner, and M. Ulm, Sound Waves and the Absence of Galilean Invariance in Flocks, *Phys. Rev. Lett.* **80**, 4819 (1998).
- [12] J. Toner and Y. Tu, Flocks, herds, and schools: A quantitative theory of flocking, *Phys. Rev. E* **58**, 4828 (1998).
- [13] G. Grégoire and H. Chaté, Onset of Collective and Cohesive Motion, *Phys. Rev. Lett.* **92**, 025702 (2004).
- [14] H. Chaté, F. Ginelli, and R. Montagne, Simple Model for Active Nematics: Quasi-Long-Range Order and Giant Fluctuations, *Phys. Rev. Lett.* **96**, 180602 (2006).
- [15] S. Ramaswamy, R. A. Simha, and J. Toner, Active nematics on a substrate: Giant number fluctuations and long-time tails, *Europhys. Lett.* **62**, 196 (2003).
- [16] S. Mishra and S. Ramaswamy, Active Nematics are Intrinsically Phase Separated, *Phys. Rev. Lett.* **97**, 090602 (2006).
- [17] F. Ginelli, F. Peruani, M. Bär, and H. Chaté, Large-Scale Collective Properties of Self-Propelled Rods, *Phys. Rev. Lett.* **104**, 184502 (2010).
- [18] C. A. Weber, T. Hanke, J. Deseigne, S. Léonard, O. Dauchot, E. Frey, and H. Chaté, Long-Range Ordering of Vibrated Polar Disks, *Phys. Rev. Lett.* **110**, 208001 (2013).
- [19] B. Bhattacharjee and D. Chaudhuri, Re-entrant phase separation in nematically aligning active polar particles, *Soft Matter* **15**, 8483 (2019).
- [20] C. A. Weber, C. Bock, and E. Frey, Defect-Mediated Phase Transitions in Active Soft Matter, *Phys. Rev. Lett.* **112**, 168301 (2014).
- [21] A. Martín-Gómez, D. Levis, A. Díaz-Guilera, and I. Pagonabarraga, Collective motion of active brownian particles with polar alignment, *Soft Matter* **14**, 2610 (2018).
- [22] E. Sese-Sansa, I. Pagonabarraga, and D. Levis, Velocity alignment promotes motility-induced phase separation, *Europhys. Lett.* **124**, 30004 (2018).
- [23] S. Mishra, R. A. Simha, and S. Ramaswamy, A dynamic renormalization group study of active nematics, *J. Stat. Mech.: Theory Exp.* (2010) P02003.
- [24] S. Shankar, S. Ramaswamy, and M. C. Marchetti, Low-noise phase of a two-dimensional active nematic system, *Phys. Rev. E* **97**, 012707 (2018).
- [25] H. Tasaki, Hohenberg-Mermin-Wagner-Type Theorems for Equilibrium Models of Flocking, *Phys. Rev. Lett.* **125**, 220601 (2020).
- [26] D. Levis, I. Pagonabarraga, and A. Díaz-Guilera, Synchronization in Dynamical Networks of Locally Coupled Self-Propelled Oscillators, *Phys. Rev. X* **7**, 011028 (2017).
- [27] I. Theurkauff, C. Cottin-Bizonne, J. Palacci, C. Ybert, and L. Bocquet, Dynamic Clustering in Active Colloidal Suspensions with Chemical Signaling, *Phys. Rev. Lett.* **108**, 268303 (2012).
- [28] I. Buttinoni, J. Bialké, F. Kümmel, H. Löwen, C. Bechinger, and T. Speck, Dynamical Clustering and Phase Separation in Suspensions of Self-Propelled Colloidal Particles, *Phys. Rev. Lett.* **110**, 238301 (2013).
- [29] J. Palacci, S. Sacanna, A. P. Steinberg, D. J. Pine, and P. M. Chaikin, Living crystals of light-activated colloidal surfers, *Science* **339**, 936 (2013).
- [30] G. Grégoire, H. Chaté, and Y. Tu, Moving and staying together without a leader, *Physica D* **181**, 157 (2003).
- [31] Y. Fily and M. C. Marchetti, Athermal Phase Separation of Self-Propelled Particles with No Alignment, *Phys. Rev. Lett.* **108**, 235702 (2012).
- [32] J. Bialké, H. Löwen, and T. Speck, Microscopic theory for the phase separation of self-propelled repulsive disks, *Europhys. Lett.* **103**, 30008 (2013).
- [33] G. S. Redner, M. F. Hagan, and A. Baskaran, Structure and Dynamics of a Phase-Separating Active Colloidal Fluid, *Phys. Rev. Lett.* **110**, 055701 (2013).
- [34] J. Bialké, T. Speck, and H. Löwen, Crystallization in A Dense Suspension of Self-Propelled Particles, *Phys. Rev. Lett.* **108**, 168301 (2012).
- [35] A. Maitra and S. Ramaswamy, Oriented Active Solids, *Phys. Rev. Lett.* **123**, 238001 (2019).
- [36] M. Warner and E. M. Terentjev, *Liquid Crystal Elastomers*, Vol. 120 (Oxford University Press, Oxford, 2007).
- [37] X. Xing and L. Radzihovsky, Thermal fluctuations and anomalous elasticity of homogeneous nematic elastomers, *Europhys. Lett.* **61**, 769 (2003).

- [38] X. Xing and L. Radzihovsky, Nonlinear elasticity, fluctuations and heterogeneity of nematic elastomers, *Ann. Phys.* **323**, 105 (2008).
- [39] E. Ferrante, A. E. Turgut, M. Dorigo, and C. Huepe, Elasticity-Based Mechanism for the Collective Motion of Self-Propelled Particles with Springlike Interactions: A Model System for Natural and Artificial Swarms, *Phys. Rev. Lett.* **111**, 268302 (2013).
- [40] E. Ferrante, A. E. Turgut, M. Dorigo, and C. Huepe, Collective motion dynamics of active solids and active crystals, *New J. Phys.* **15**, 095011 (2013).
- [41] L. Caprini, U. M. B. Marconi, C. Maggi, M. Paoluzzi, and A. Puglisi, Hidden velocity ordering in dense suspensions of self-propelled disks, *Phys. Rev. Research* **2**, 023321 (2020).
- [42] A. M. Menzel and T. Ohta, Soft deformable self-propelled particles, *Europhys. Lett.* **99**, 58001 (2012).
- [43] M. N. Van Der Linden, L. C. Alexander, D. G. A. L. Aarts, and O. Dauchot, Interrupted Motility Induced Phase Separation in Aligning Active Colloids, *Phys. Rev. Lett.* **123**, 098001 (2019).
- [44] A. E. Turgut, H. Çelikkanat, F. Gökçe, and E. Şahin, Self-organized flocking in mobile robot swarms, *Swarm Intell.* **2**, 97 (2008).
- [45] H. Çelikkanat and E. Şahin, Steering self-organized robot flocks through externally guided individuals, *Neural Comput. Appl.* **19**, 849 (2010).
- [46] E. Ferrante, A. E. Turgut, N. Mathews, M. Birattari, and M. Dorigo, Flocking in stationary and non-stationary environments: A novel communication strategy for heading alignment, in *Proceedings of the International Conference on Parallel Problem Solving from Nature* (Springer, Berlin, 2010), pp. 331–340.
- [47] C. Huepe, E. Ferrante, T. Wenseleers, and A. E. Turgut, Scale-free correlations in flocking systems with position-based interactions, *J. Stat. Phys.* **158**, 549 (2015).
- [48] P. E. Kloeden and E. Platen, *Numerical Solution of Stochastic Differential Equations*, Vol. 23 (Springer Science & Business Media, New York, 2013).
- [49] Y.-W. Li and M. P. Ciamarra, Accurate determination of the translational correlation function of two-dimensional solids, *Phys. Rev. E* **100**, 062606 (2019).
- [50] P. M. Chaikin, T. C. Lubensky, and T. A. Witten, *Principles of Condensed Matter Physics*, Vol. 10 (Cambridge University Press, Cambridge, UK, 1995).
- [51] L. Caprini, U. M. B. Marconi, and A. Puglisi, Spontaneous Velocity Alignment in Motility-Induced Phase Separation, *Phys. Rev. Lett.* **124**, 078001 (2020).
- [52] L. Caprini and U. M. B. Marconi, Spatial velocity correlations in inertial systems of active brownian particles, *Soft Matter* **17**, 4109 (2021).
- [53] T. C. Adhyapak, S. Ramaswamy, and J. Toner, Live Soap: Stability, Order, and Fluctuations in Apolar Active Smectics, *Phys. Rev. Lett.* **110**, 118102 (2013).
- [54] L. Chen, J. Toner *et al.*, Universality for Moving Stripes: A Hydrodynamic Theory of Polar Active Smectics, *Phys. Rev. Lett.* **111**, 088701 (2013).
- [55] C. Scheibner, A. Souslov, D. Banerjee, P. Surówka, W. T. M. Irvine, and V. Vitelli, Odd elasticity, *Nat. Phys.* **16**, 475 (2020).
- [56] J. Zhang, R. Alert, J. Yan, N. S. Wingreen, and S. Granick, Active phase separation by turning towards regions of higher density, *Nat. Phys.* **17**, 961 (2021).
- [57] D. Martin, J. O’Byrne, M. E. Cates, É. Fodor, C. Nardini, J. Tailleur, and F. van Wijland, Statistical mechanics of active ornstein-uhlenbeck particles, *Phys. Rev. E* **103**, 032607 (2021).
- [58] L. D. Landau and E. M. Lifshitz, *Theory of Elasticity*, 3rd ed. (Butterworth-Heinemann, New York, 1986).
- [59] A. L. Fetter and J. D. Walecka, *Theoretical Mechanics of Particles and Continua* (Courier Corporation, New York, 2003).
- [60] W. G. Hoover, W. T. Ashurst, and R. J. Olness, Two-dimensional computer studies of crystal stability and fluid viscosity, *J. Chem. Phys.* **60**, 4043 (1974).
- [61] J. M. Kosterlitz and D. J. Thouless, Ordering, metastability and phase transitions in two-dimensional systems, *J. Phys. C: Solid State Phys.* **6**, 1181 (1973).
- [62] A. M. Lyapunov, The general problem of the stability of motion, *Int. J. Contr.* **55**, 531 (1992).